Title:

Mitochondrial heterogeneity disrupts osteoclast differentiation and bone resorption by impairing respiratory complex I

Houfu Leng[1, #], Jiahao Jiang [2, #], Katja Gassner[3], Swati Midha[1,4,5,6], Raquel Justo-Méndez[3], Jianqing Zheng[1], Timothy Hall[7], Lin Luo[1,8], Suzanne D West[9], Tonia L. Vincent[1], Angus Wann[1,4], Kashyap A Patel[7], Joanna Poulton[10], Chris A. O'Callaghan[2], Ana Victoria Lechuga-Vieco[1,3,12], Anna Katharina Simon[1,11,12]

[1-] Kennedy Institute of Rheumatology, University of Oxford, Roosevelt Drive, Oxford, OX3 7FY, UK.

[2-] Centre for Human Genetics, Nuffield Department of Medicine, Wellcome Centre for Human Genetics, University of Oxford, United Kingdom.

[3-] Institute for Research in Biomedicine (IRB Barcelona). The Barcelona Institute of Science and Technology, Baldiri Reixac, 10, 08028 Barcelona, Spain

[4-] School of Biological Sciences, University of Southampton, Southampton, Hampshire, SO17 1BJ UK

[5-] Centre for Predictive In Vitro Models, Queen Mary University of London, UK

[6-] Centre for Bioengineering, School of Engineering and Materials Science, Queen Mary University of London, UK

[7-]Department of Clinical and Biomedical Sciences, Faculty of Health and Life Sciences, University of Exeter, Exeter, UK.

[8-] CAMS Oxford Institute, Nuffield Department of Medicine, University of Oxford, Oxford, UK

[9-] NHS Highly Specialised Service for Rare Mitochondrial Disorders, Oxford Centre for Genomic Medicine, Oxford University Hospitals, Oxford, UK

[10-] Department of Women's and Reproductive Health, The Women's Centre, University of Oxford, Oxford, United Kingdom

[11-] Max-Delbrück-Center for Molecular Medicine, Berlin, Germany

[12-] Corresponding Authors

[#] Contributed equally

Summary:

Mitochondria are required to meet the high energy demands of osteoclast differentiation and adapt to hypoxia, inflammatory signals and oxidative stress. Heteroplasmy, the coexistence of different mitochondrial DNAs (mtDNAs) in one cell disrupts energy balance and causes metabolic stress. Using a genetically engineered mouse model, we demonstrate that heteroplasmy impairs osteoclast differentiation and subsequently reduces bone resorption. Mechanistically, we find that heteroplasmic cells accumulate complex I subunits of the electron transport chain in the cytoplasm, which severely disrupts ATP production and leads to premature termination of osteoclastogenesis. Importantly, we show that stimulating autophagy and improving mitochondrial quality using spermidine alleviates the dysfunction in both the murine heteroplasmic model and in human heteroplasmic osteoclasts carrying m.3242A>G mutations, partially through enhanced mitochondrial selection. Overall, our work highlights the role of mtDNA in osteoclast function and introduces potential therapeutic approaches for mitochondrial and bone disorders.

Keywords: Complex I, osteoclasts, mitochondrial DNA, heteroplasmy, spermidine, autophagy

Graphical Abstract

48

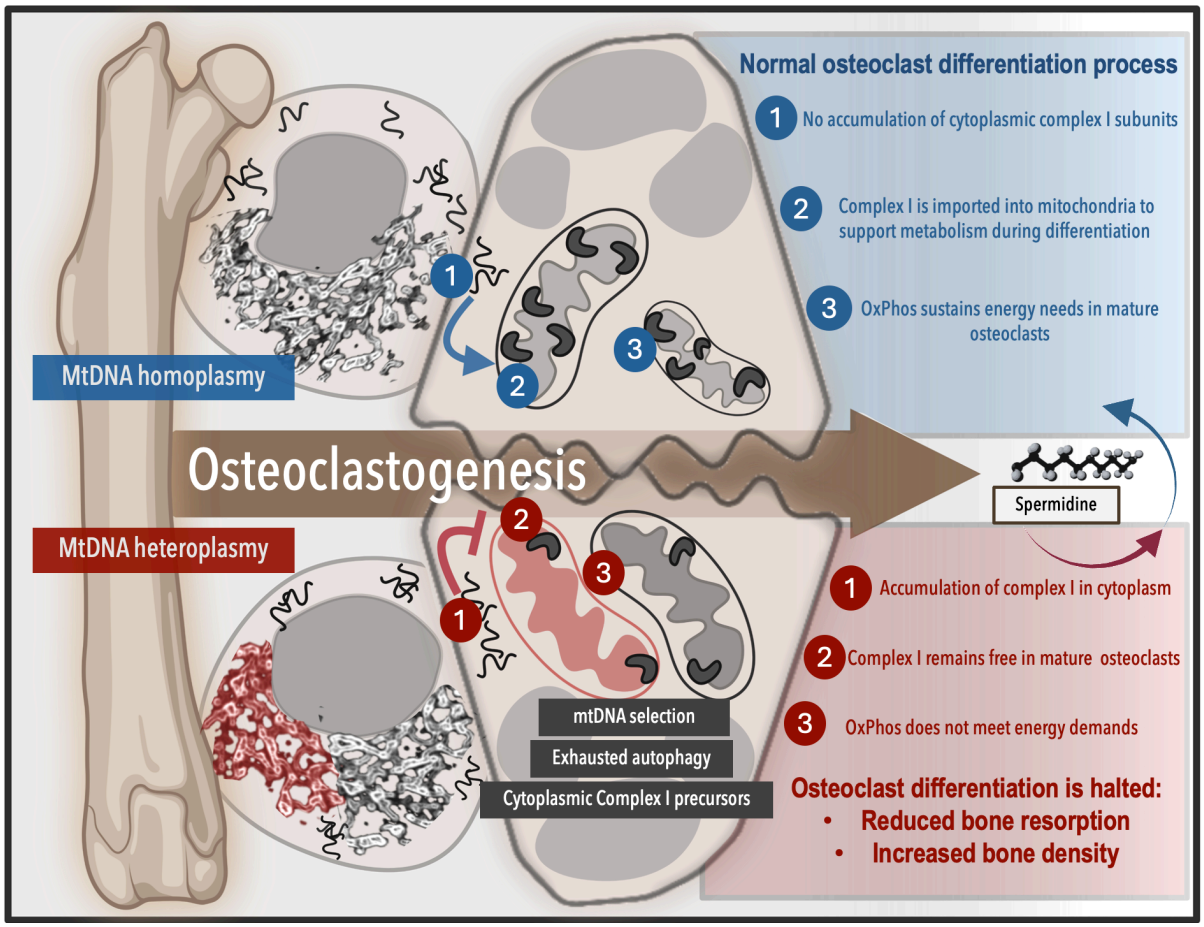
Normal osteoclast differentiation process
1 No accumulation of cytoplasmic complex I subunits
2 Complex I is imported into mitochondria to support metabolism during differentiation
3 OxPhos sustains energy needs in mature osteoclasts
MtDNA homoplasmy
Osteoclastogenesis
Spermidine
MtDNA heteroplasmy
mtDNA selection
Exhausted autophagy
Cytoplasmic Complex I precursors
1 Accumulation of complex I in cytoplasm
2 Complex I remains free in mature osteoclasts
3 OxPhos does not meet energy demands
Osteoclast differentiation is halted:
• Reduced bone resorption
• Increased bone density

49

Introduction

Skeletal homeostasis relies on a network of cells in the bone, namely the bone matrix synthesizing osteoblasts (OB) and the bone resorbing osteoclasts (OC). OC are terminally differentiated multinucleated cells originating from myeloid progenitors in the bone marrow. Engagement of RANKL (receptor activator of nuclear factor kappa-B ligand) mainly secreted by OBs with its cognate receptor RANK expressed on OC precursor cells is required for mature OC formation[1]. OC are vital for bone remodeling, deficiency of which can cause osteopetrosis whilst overactivation can cause osteoporosis or Paget Disease[2]. The demanding environmental conditions during osteoclastogenesis require robust metabolic activity to support differentiation and function[3]. Disruptions in the energy metabolism during OC differentiation cause an imbalance in skeletal homeostasis, leading to the onset and progression of bone-related diseases[3]. The energy required for OC differentiation mainly derives from glycolysis and mitochondrial oxidative metabolism[4,5]. Additionally protons (H+) generated by ATP hydrolysis are required to support acidification and bone collagen degradation[6,7].

The generation of new mitochondrial DNA and proteins has been linked to OC differentiation and function. Indeed, mature OCs have bigger and a larger number of mitochondria, elevated mitochondrial oxygen consumption rates and higher levels of the electron transport chain enzymes[4,8]. Notably, RANKL, has been shown to stimulate mitochondrial biogenesis[8,9] . The extensive transcriptional and metabolic reprogramming and intact mitochondrial function are essential for osteoclast differentiation and to demineralize the bone. The absence of Ndufs4, a subunit of complex I in the mitochondrial electron transport chain (mtETC) encoded by the nuclear genome, has been associated with impaired osteoclast differentiation and function, leading to increased bone density[10]. In addition, it has been reported that ECSIT, a complex I-associated protein, plays a central role in the mitochondrial response to early signaling of RANKL[9].

Although the role of mitochondria in osteoclasts (OCs) is well established, it remains unclear how OCs adapt to mutated mitochondrial DNA (mtDNA). This adaptation becomes particularly relevant in the context of heteroplasmy, the coexistence of multiple mtDNA variants within a cell. Bone tissue generally exhibits low levels of heteroplasmy, which may contribute to the limited research on the functional impact of mtDNA variation in bone-residing cells[11]. While mitochondrial point mutations are present in healthy individuals they are commonly associated with mitochondrial diseases. The pathological m.3243A>G mitochondrial point mutation in the MT-TL1 gene was first identified three decades ago and causes the MELAS syndrome (mitochondrial encephalopathy with lactic acidosis and stroke-like episodes)[12,13]. Over time, a better understanding of the disease has revealed an expanding spectrum of extra-neurological manifestations[14]. Primary mitochondrial diseases have been associated with poor bone health[15] and hearing loss due to the temporal bone structure damage, which has been observed in MELAS disease[16,17]. However, due to the complex genetics, phenotypic variability of the disease, and pathogenic molecular mechanisms being unclear, these associations are difficult to ascertain. To study mitochondrial diseases, the genetic modification of

90 mitochondrial DNA in mammalian cells would be ideal but this is still highly challenging[18]. To
91 overcome this, a heteroplasmic mouse model was developed on the C57BL/6 background,
92 carrying a variable mixture of two mtDNA variants, C57 and NZB. NZB mtDNA differs from C57
93 mtDNA by several mitochondrial single nucleotide polymorphisms (SNPs), including 12
94 missense mutations, 4 tRNA mutations, 8 rRNA mutations, and 10 mutations in non-coding
95 regions, making the NZB variant more efficient at oxidative phosphorylation[19]. When both
96 variants coexist, cells selectively retain the preferred mitochondria, leading to varying degrees
97 of heteroplasmy across different tissues and cell types[20]. This process of mitochondrial
98 selection in postnatal individuals closely mirrors the mutant load distribution observed in
99 tissues affected by primary mitochondrial diseases[11].

100 Here we address how mtDNA variability impacts osteoclastogenesis both *in vivo* and *ex vivo*,
101 using bone marrow samples from heteroplasmic mice and peripheral blood mononuclear cells
102 (PBMCs) from m.3243A>G patients. We find that mitochondrial DNA heterogeneity in mice
103 leads to increased bone density attributed to impaired OC formation and function.
104 Heteroplasmic osteoclasts exhibit impaired function due to reduced oxidative phosphorylation
105 and ATP production, resulting from the failure of nuclear-encoded complex I subunits to be
106 imported into mitochondria during the early stages of OC differentiation. We show that
107 preserving mitochondrial quality through spermidine treatment enhances osteoclast
108 differentiation from m.3243A>G patients *ex vivo* and restores osteoclast function in
109 heteroplasmic mice. Our study highlights the crucial role of preserving mitochondrial function
110 under conditions of mtDNA heterogeneity to maintain skeletal homeostasis. This offers a
111 promising strategy for treating age-related and mitochondrial disease-associated bone
112 pathologies.

113

114 ## Results

115 ### BL/6$^{C57\text{-}NZB}$ mice exhibit increased bone density due to diminished osteoclast function

116 To investigate if BL/6$^{C57\text{-}NZB}$ mice display changes in their bone mass, tibiae were collected from
117 aged-matched male BL/6^{C57}, BL/6^{NZB} and BL/6$^{C57\text{-}NZB}$ mice for micro-CT analysis. BL/6$^{C57\text{-}NZB}$ mice
118 showed an increase in trabecular bone (Fig. 1A). Accordingly, when we quantified bone
119 parameters, we found a 1.3-fold increase of bone volume over total volume (BV/TV) and a 1.2-
120 fold increase of trabecular thickness (Tb. Th), accompanied by a significant decrease in bone
121 surface density (BS/BV) and in trabecular separation (Tb. Sp). The decrease in the BS/BV ratio
122 in BL/6$^{C57\text{-}NZB}$ group was due to a significant increase in BV, as compared to BS. (Fig. 1B-C).
123 Furthermore, a significant increase of cortical thickness (Ct. Th) and cortical area (Ct. Ar) was
124 observed in BL/6$^{C57\text{-}NZB}$ group (Fig1. C), confirming an increase of the overall bone parameters.
125 Next, we investigated whether these increased bone parameters lead to a corresponding
126 increase in bone strength by measuring resistance to fracture. We conducted biomechanical
127 compression testing of the femur from BL/6^{C57} mice, BL/6^{NZB} mice and BL/6$^{C57\text{-}NZB}$ mice (Fig. 1D).
128 Compared with bones from BL/6^{C57} mice, those from BL/6$^{C57\text{-}NZB}$ mice needed 25% more

129 maximum load to break (Fig. 1D). Therefore, the femur from BL/6$^{C57\text{-}NZB}$ had increased bone
130 mechanical strength, resulting in greater resistance to deformation or fracture. This phenotype
131 may stem from reduced osteoclast-mediated bone resorption or enhanced osteoblast-driven
132 bone formation.

133 We first investigated whether bone-resorbing OCs are affected in BL/6$^{C57\text{-}NZB}$ mice, longitudinal
134 cross-sections of tibiae were stained with tartrate-resistant acid phosphatase (TRAP) specific
135 for OC. According to bone histomorphometry, tibiae from BL/6$^{C57\text{-}NZB}$ mice had significantly
136 lower signal for TRAP-positive OC when compared to those from BL/6^{C57} control mice (Fig. 1E-
137 F). Consistently, a significant reduction of serum carboxy-terminal cross-linked telopeptide of
138 type 1 collagen (CTX-1) level was observed in BL/6$^{C57\text{-}NZB}$ mice, indicating that a lower level of
139 systemic OC activity and of bone resorption (Fig. 1G). However, no difference was observed in
140 the frequency of bone marrow OC precursors as demonstrated by expression of surface
141 markers (CD11b^{-}CD3^{-}B220^{-}CD115^{+}) between the 3 genotypes, indicating a diminished OC
142 differentiation from BL/6$^{C57\text{-}NZB}$ OC precursors (Supplementary Fig. 1A). No differences were
143 observed in serum PINP (serum procollagen type I N-propeptide), an osteoblast-derived
144 marker reflecting bone formation, among the three groups, suggesting that the observed
145 increases in bone volume and strength in BL/6$^{C57\text{-}NZB}$ mice were due to decrease in OC number
146 and function rather than an increase in osteoblast formation (Fig. 1G).

147 To confirm that OC and not OB mediate the bone phenotype, we performed bone marrow
148 chimera experiments, in which the host provides the OB and the donor the OC, as the latter
149 are of hematopoietic origin. Lethally irradiated BL/6$^{C57\text{-}NZB}$and BL/6^{C57} mice were transplanted
150 with BM donor cells from either BL/6^{C57} or BL/6$^{C57\text{-}NZB}$ mice. Bone marrow engraftments were
151 monitored by bleeding every 2 weeks, with the donor cells expressing the CD45.2 isoform while
152 the host was CD45.1^{+} to track donor and host cells (Supplementary Fig. 1B–C). Notably, we
153 found increased bone density, as measured by BV/TV micro-CT analysis (Fig. 1H-I and
154 Supplementary Fig. 1D), regardless of the recipient strain. These findings indicate that the
155 increased bone volume in BL/6$^{C57\text{-}NZB}$ mice is driven by impaired differentiation and function of
156 OC which are of hematopoietic origin.

157 **Osteoclastogenesis is significantly compromised during the first days of the differentiation**
158 **process in heteroplasmic cells**

159 To determine the extent to which osteoclastogenesis contributes to the phenotype observed
160 in BL/6$^{C57\text{-}NZB}$ mice, we conducted *in vitro* OC differentiation assays. Bone marrow cells from
161 the three strains were cultured *in vitro* for 2 days with murine macrophage colony stimulating
162 factor (M-CSF) to generate macrophages (day 0), followed by culture with murine M-CSF and
163 RANKL for 5 days to induce OC formation. Notably, bone marrow cells from BL/6$^{C57\text{-}NZB}$ mice
164 showed a significant reduction in TRAP-positive OC formation (Fig. 2A)[1].

165 To understand the molecular mechanisms underlying the differences in osteoclastogenic
166 capacity across the different mitochondrial genotypes we conducted single-cell RNA
167 sequencing (scRNA-seq) at various stages of OC differentiation (Fig. 2B). Bone marrow cells

168 from the three strains were cultured for 2 days with M-CSF to generate macrophages (day 0),
169 followed by culture with M-CSF and RANKL for either 1 day or 3 days to induce OC formation.
170 Successful *in vitro* OC differentiation was validated by cross-referencing reported marker genes
171 (e.g *Acp5* and *Ctsk* in Fig. 2C) and negative regulators of OCs following RANKL treatment (e.g.
172 *Irf8* and *Mafb*)[1] (Supplementary Fig.2A). After applying quality control filters, we analyzed a
173 total of 10,809 cells, comprising 4,028, 3,742 and 3,039 cells on day 0, day 1 and day 3,
174 respectively (Fig. 2D and Fig. 2E). Unsupervised graph-based clustering of these single-cell
175 transcriptomic profiles defined 9 distinct cell populations, including a monocyte-like precursor
176 population and a terminal osteoclast population (Fig. 2D). Other transitional populations
177 included *Cxcl16*^{hi} macrophages, dendritic cells, early- and late-stage pre-osteoclasts, and three
178 proliferative populations (Fig. 2D).

179 To further infer the linkage between each cell population, we computed a per-cell latent time
180 (Supplementary Fig. 2B) and performed partition-based graph abstraction (PAGA) analysis
181 based on the RNA-velocity dynamics[21,22] (Supplementary Fig. 2C) . These analyses revealed a
182 cell trajectory during osteoclastogenesis, which progresses from monocytic precursors to
183 osteoclasts, passing through *Cxcl16*^{hi} macrophages, early-stage pre-osteoclasts and late-stage
184 pre-osteoclasts (Supplementary Fig. 2B-C). Along this trajectory, we noted that BL/6$^{C57\text{-}NZB}$ cells
185 were relatively concentrated in Cxcl16^{hi} macrophages (17.4%), and early-stage pre-osteoclasts
186 (8.0%) compared to homoplasmic BL/6^{C57} (14.0% and 6.5%) or BL/6^{NZB} (14.3% and 6.5%) cells.
187 Consequently, fewer heteroplasmic cells reached the mature osteoclast population (10.2%
188 compared to 14.7% and 14.9% in BL/6^{C57} and BL/6^{NZB} cells, respectively) (Fig. 2E and
189 Supplementary Fig. 2D). The statistical significance of this observation was further validated
190 by differential abundance testing using MiloR [23] (Supplementary Fig. 2D).

191 Since osteoclastogenesis requires finely tuned cellular adaptive mechanisms[24], we
192 hypothesized that heteroplasmic results in the generation of reduced numbers of mature cells
193 and these are functionally compromised compared to control BL/6^{C57} osteoclasts. Indeed,
194 pathway enrichment analysis revealed key differences in cellular respiration between the
195 genotypes, including downregulation of the tricarboxylic acid cycle and of mitochondria-
196 related functional pathways in differentiated osteoclasts (Fig. 2F). Additionally, there was a
197 downregulation of cellular responses to hypoxic environments and associated oxidative stress,
198 particularly reactive oxygen species. The lack of cellular adaptation to the demanding
199 conditions occurring during the early days of OC differentiation was further validated by the
200 fact that BL/6$^{C57\text{-}NZB}$ cells exhibit increased catabolic metabolism, despite the findings that
201 adaptation to hypoxia in OC maturation typically requires enhanced cellular anabolism[25] (Fig.
202 2F). Collectively, our findings suggest that heteroplasmic cells face challenges in
203 osteoclastogenesis, leading to premature arrest at the macrophage stage, which may be linked
204 to altered metabolic adaptation and pathway dysregulation.

205 **Alterations in complex I in heteroplasmic cells impair oxidative phosphorylation and**
206 **metabolic adaptation during osteoclast differentiation.**

207 We began with the premise that BL/6^{C57}, BL/6^{NZB} and BL/6$^{C57\text{-}NZB}$ cells share the same nuclear
208 genome but differ in mitochondrial DNA, and that changes in nucleo-mitochondrial crosstalk
209 could lead to alterations in the mitochondrial electron transport chain[20]. Since mitochondria
210 serve as a central metabolic hub, we analyzed gene expression of major metabolic pathways
211 during OC differentiation. At day 0 of *in vitro* OC differentiation, there were no significant
212 differences in metabolic pathways of BL/6$^{C57\text{-}NZB}$ cells compared to wild-type BL/6^{C57}; only few
213 pathways, including glycolysis, were upregulated at day 1 upon RANKL treatment in BL/6$^{C57\text{-}NZB}$
214 cells (Fig. 3A and Supplementary Fig. 3A). In contrast, after 3 days of differentiation, most
215 mitochondrial-associated pathways, including glutamate degradation pathway, adenosine
216 biosynthesis, galactose metabolism, pentose phosphate metabolism, ketogenesis, Krebs cycle,
217 and pyrimidine biosynthesis, were downregulated in the OC cultures from BL/6$^{C57\text{-}NZB}$ mice (Fig.
218 3A and Supplementary Fig. 3A). Specifically, we evaluated the activation of the oxidative
219 phosphorylation (OXPHOS) pathway by aggregating the average gene expression of all involved
220 genes (n = 107 genes as annotated in the KEGG database). OC differentiation increased the
221 cellular energy demand, as indicated by the elevated OXPHOS scores in pre-osteoclasts and
222 mature osteoclasts (Fig. 3B). The significant reduction in the OXPHOS score observed in OCs
223 (Cluster 2, representing the most mature osteoclastic cells) derived from BL/6$^{C57\text{-}NZB}$ cells
224 suggests a disruption in oxidative phosphorylation and potentially compromised mitochondrial
225 metabolic performance (Fig. 3B).

226 To validate the scRNA-seq findings, we used Seahorse technology to assess the oxygen
227 consumption rate in BL/6^{C57}, BL/6^{NZB} and BL/6$^{C57\text{-}NZB}$ cells (Fig. 3C and Supplementary Figure 3B).
228 Consistent with gene expression data, no differences were observed at day 0. However, by day
229 1 of OC differentiation, cells from BL/6$^{C57\text{-}NZB}$ mice exhibited a reduction in maximal
230 mitochondrial respiratory capacity (Fig. 3C and Supplementary Figure 3B) alongside an increase
231 in reactive oxygen species (ROS) and in mitochondrial mass, likely as a compensatory response
232 (Supplementary Figure 3C-D). These results provide further evidence of a compromised
233 OXPHOS capacity in heteroplasmic cells early in the OC differentiation process. However, by
234 day 3 following RANKL treatment, heteroplasmic cells exhibit lower mitochondrial mass while
235 maintaining the same spare respiratory capacity (SRC) (Supplementary Figure 3B-C), likely by
236 utilizing alternative substrates and relying on complex II (succinate dehydrogenase)[26]. We
237 analyzed the expression of selected OXPHOS structural subunits by western blot on days 0, 1,
238 2, 3, and 5 of OC differentiation. Interestingly, each genotype displayed a distinct temporal
239 pattern in the relative abundance of the proteins analyzed. Thus, wild-type BL/6^{C57}cells,
240 showed a sequential increase in NDUFB8 (complex I) and SDHB (complex II) expression levels
241 during differentiation with a peak at day 3 (Supplementary Figure 3E). UQCR2 (complex III) and
242 MTCOI (CIV) changes are less prominent, remaining elevated all the period. Finally, ATP5A
243 (complex V) peaked acutely at day 5 (Supplementary Figure 3E). On the other hand, BL/6^{NZB}
244 cell differentiation resemble that of the previous cells with a sharpen peak of SDHB at day 3
245 and less intense ATP5A increase (Supplementary Figure 3E). In contrast, BL/6$^{C57\text{-}NZB}$ cells
246 showed a mitigated response in NDUFB8 expression after day 3 (Supplementary Fig. 3E),
247 supporting previous findings (Fig. 3A). Heteroplasmic cells also showed a very mild increase in

248 SDHB expression. Together these differences lead to a relevant drop in the relative activation
249 between complex II and complex I representative proteins. Very interestingly, these changes
250 in expression correlated with the significantly higher complex I/II activity ratio characteristic of
251 day 3 BL/6$^{C57-NZB}$ cells (Fig. 3D). We then address how this differentiation impacted on ATP
252 synthesis and found that BL/6$^{C57-NZB}$ cells exhibited reduced efficiency in ATP production (Fig.
253 3E). This analysis examined changes in expression on a per-cell basis. Interestingly, when
254 analyzed per mitochondria, heteroplasmic cells show lower levels of NDUFA9, an nDNA-
255 encoded subunit of respiratory complex I, compared to BL/6^{C57} and BL/6^{NZB}, after day 3 of *in*
256 *vitro* OC differentiation. (Fig. 3F-G). In contrast, ATPβ, a subunit of Complex V (ATPase)
257 responsible for ATP synthesis, showed no differences between genotypes in expression per
258 mitochondrion on day 3 across the different genotypes (Fig. 3F-G). Altogether, the data suggest
259 that dysregulation of complex I may be the primary factor affected in OC differentiation in
260 heteroplasmic cells.

261 **OC differentiation requires sequential import of complex I subunits**

262 Thus, complex I became a key focus of our analysis as it also harbors 14 of the SNPs between
263 the C57 and NZB haplotypes[19].

264 The upregulation of genes encoded in the mitochondrial genome is not apparent from day 0
265 to day 1 but becomes evident between day 1 and day 3 in cells derived from wild-type BL/6^{C57}
266 mice (Supplementary Fig. 4A). Nuclear-encoded mitochondrial proteins are synthesized by
267 cytosolic ribosomes as precursors and need to be imported into mitochondria[27]. Among them,
268 the complex I subunit NDUFA9 harbors an N-terminal cleavable pre-sequence that facilitates
269 its mitochondrial targeting[28]. We used confocal imaging to determine whether nuclear-
270 encoded subunits of the respiratory complexes were properly imported and successfully
271 assembled into functional respiratory complexes within mitochondria. Strikingly, we observed
272 that a significant proportion of NDUFA9 subunit remains in the cytoplasm on day 1 of
273 differentiation of OC from wild-type BL/6^{C57} BL/6^{NZB} and BL/6$^{C57-NZB}$ mice (Supplementary Fig.
274 4B). Intriguingly, from day 3 to day 5, the colocalization of complex I with mitochondria
275 increases in wild-type cells, suggesting that greater complex I respiratory complex formation is
276 required during OC development (Fig. 4A-B). However, this increase does not happen to the
277 same extent in BL/6$^{C57-NZB}$ cells (Fig 4B). By day 5, this colocalization decreases, and prominent
278 localization of the nDNA-encoded subunit within mitochondria is observed only in wild-type
279 BL/6^{C57} osteoclasts (Fig. 4B).

280 Previous studies indicate that complex I inhibition disrupts mitochondrial protein import,
281 impairs chaperone function, and activates the mitochondrial unfolded protein response
282 (mtUPR) to prevent aggregation of respiratory complex subunits[29]. The analysis of gene
283 expression changes related to the mitochondrial protein import machinery and mitochondrial
284 degradome at day 3 of OC differentiation revealed their pronounced downregulation in
285 BL/6$^{C57-NZB}$ cells compared to BL/6^{C57} cells (Fig. 4C-D). Some of our previous data already
286 indicate a downregulation of the assembly proteins for respiratory complex I (Figure 2F),

287 suggesting that the failure to complete protein import into mitochondria leads to decreased
288 respiratory complex assembly factors in BL/6$^{C57\text{-}NZB}$ cells compared to BL/6^{C57} (Fig. 4E).

289 Altogether, nuclear-encoded complex I subunits fail to be either imported into mitochondria
290 or properly degraded in the cytoplasm during OC differentiation in BL/6$^{C57\text{-}NZB}$. Both processes
291 require ATP[27,30,31], which is reduced with heteroplasmy at the stage when OCs would normally
292 depend on respiratory complex I formation for mitochondrial function.

293 **Mitochondrial selection in heteroplasmic cells is evident during osteoclastogenesis**

294 We previously reported that mitochondrial heteroplasmy can be resolved through non-
295 random mtDNA segregation specific to tissue and cell types[20]. Considering the substantial
296 changes in metabolic profiles during osteoclastogenesis[32], we reasoned that the successfully
297 differentiated osteoclasts might not represent the same heteroplasmic levels as compared to
298 monocytic precursors. To genotype mitochondrial variants at single-cell resolution during early
299 stages of OC differentiation, we adapted the mgatk pipeline[33] with deep sequencing of the
300 scRNA-seq libraries. Due to the relatively low coverage for individual variants, we aggregated
301 all NZB mtDNA SNPs and calculated an overall mtDNA NZB percentage for each single cell on
302 day 1 and day 3 of *in vitro* OC differentiation of cells from BL/6$^{C57\text{-}NZB}$ mice. Cells with low
303 coverage were subsequently filtered out, leaving an average of 237 sequencing reads per cell
304 covering any NZB mtDNA variants (Supplementary Fig. 5A). We observed a higher level of NZB
305 mtDNA transcripts on day 3 compared to day 1 cells, which was independent of the sequencing
306 depth (Fig. 5A). The percentage of NZB mtDNA slightly increased along the OC differentiation
307 trajectory (Supplementary Fig. 5B). We further validated these findings using PCR followed by
308 RFLP (Restriction Fragment Length Polymorphism) analysis in OC cultures at Days 1 and 3. We
309 targeted the G4276A nucleotide, which forms part of a BamH1 restriction site in C57 mtDNA
310 that is absent in NZB mtDNA[34,35,36]. Our data showed a shift toward more NZB mtDNA as OC
311 differentiation progressed (Fig. 5B & Supplementary Fig. 5C). In line with these results, single-
312 cell mitochondrial genotyping demonstrates the heterogeneity of mitochondrial heteroplasmy
313 across different clusters, with mature osteoclasts showing significant enrichment for the NZB
314 mtDNA haplotype (Fig. 5C).

315 **Heteroplasmy leads to exhausted autophagy and OC maturation can be rescued by**
316 **restoring spermidine levels**

317 The downregulation of the mitochondrial proteases seen in the OC degradome analysis in
318 heteroplasmic OC cultures (Fig. 4D) may lead to impaired organelle quality control. To
319 determine whether the selective removal of mitochondria with distinct mtDNA haplotype
320 profiles within the cytoplasm of BL/6$^{C57\text{-}NZB}$ cells affects mitochondrial recycling during
321 osteoclastogenesis, we analyzed the autophagic flux throughout the OC differentiation process.
322 On day 1, BafA1 treatment increased LC3-II levels and decreased the LC3-I/LC3-II ratio,
323 indicating strong autophagic flux across all genotypes (Fig. 5D–E). However, by day 3, BafA1,
324 that was used to block autophagosome-lysosome fusion and assess autophagy flux, no longer
325 increased LC3-II in BL/6$^{C57\text{-}NZB}$ cells (Fig. 5D–E). This, together with elevated p62 levels in

326 heteroplasmic cells, even in the absence of BafA1 (Supplementary Fig. 5D), suggests a block in
327 autophagic flux at day 3. Consistent with this, the expression of *Tfeb,* a key transcription factor
328 involved in autophagy[37] and in the regulation of respiratory complex I[38] was downregulated
329 from monocyte precursors to OCs in *in vitro* OC differentiation cultures derived from both
330 BL/6^{C57} and BL/6^{NZB} mice, but not from BL/6$^{C57\text{-}NZB}$ mice (Supplementary Fig. 5E). Overall, this
331 suggests that autophagy is regulated differently with heteroplasmy over the course of
332 differentiation and may contribute to the metabolic phenotype of heteroplasmic OC.

333 Next, we reasoned that the metabolite spermidine may enhance differentiation of
334 heteroplasmic OCs. We have previously demonstrated that autophagy is regulated by
335 endogenous spermidine levels which control translation of TFEB [39,40]. Spermidine activates
336 mitochondrial translation in myeloid cells[41], and boosts oxidative metabolism by binding to the
337 mitochondrial trifunctional protein (MTP) in T cells[42]. Spermidine given to mice in the drinking
338 water restores autophagy levels when these are low[37]. First, we performed OC differentiation
339 of cells from heteroplasmic mice with spermidine supplementation in the media. Spermidine
340 restored osteoclast formation *in vitro* in heteroplasmic cells compared to untreated cultures
341 (Fig. 5F-G). We also observed a significant increase in NZB mtDNA selection on day 5 (Fig. 5H)
342 without any change in mtDNA content (Supplementary Fig. 5F). The dose used to observe this
343 phenotype in heteroplasmic cells has previously been shown to inhibit OC formation in wild-
344 type cells[43], a finding we reproduced in our analyses (Fig. 5F).

345 While no changes in total ATP were observed in the spermidine-treated OC cultures on day 1
346 of differentiation (Supplementary Fig. 5G), treated heteroplasmic cells showed a sharp
347 increase in ATP content on day 3 (Fig. 5I). We observed an increase in mitochondrial complex
348 I expression through confocal imaging in spermidine-treated versus untreated OC cultures
349 from BL/6$^{C57\text{-}NZB}$ mice on day 5 (Fig. 5J & Supplementary Fig. 5H-I).

350 To investigate if spermidine can modulate the phenotype of heteroplasmic OC *in vivo*, we
351 generated BM chimeric mice by transplanting BM donor cells from wild-type BL/6^{C57} or BL/6$^{C57\text{-}}$
352 ^{NZB} mice into lethally irradiated BL/6$^{C57\text{-}NZB}$ recipients, ensuring that all recipient mice share the
353 same host tissue background and avoiding differences in the host environment that could
354 influence the phenotype. After 8 weeks of spermidine treatment (5 mM in drinking water),
355 bone phenotyping analyses using micro-CT demonstrate that in BL/6$^{C57\text{-}NZB}$ BM donor cells
356 spermidine administration led to a decrease of BV/TV in mice, accompanied by an increase in
357 Tb. Sp, confirming an activation of bone catabolism (Fig. 5K-L). Lastly, spermidine-treated
358 chimeric BL/6$^{C57\text{-}NZB}$ mice showed decreased bone mechanical strength, reversing the
359 phenotype to resemble wild-type BM (Fig. 5M). Taken together, OC differentiation in
360 heteroplasmic cells is linked to a shift in mitochondrial heteroplasmy toward NZB mtDNA
361 variants. By restoring spermidine levels that may have been depleted due to the extra demand
362 during differentiation, osteoclastogenesis was restored, both *in vitro* and *in vivo*.

363 **m.3243A>G heteroplasmy disrupts human osteoclast differentiation, which can be**
364 **restored by spermidine**

365 To evaluate the potential for osteoclast formation of cells from people with heteroplasmic
366 mitochondrial disease, we collected blood from middle-aged people with MELAS carrying both
367 healthy and m.3243A>G mutated mtDNA within their cytoplasm. This mutation has been linked
368 previously to bone abnormalities[44]. Using peripheral blood mononuclear cells (PBMCs) from
369 age- and sex-matched healthy donors and people with m.3243A>G heteroplasmy, we
370 established an *in vitro* OC differentiation experiment. Briefly, human PBMCs were isolated on
371 day -3 and were seeded with human M-CSF. On day 0, the cells were induced to differentiate
372 into OCs using human M-CSF and human RANKL. By day 6, mature osteoclasts had formed and
373 were fixed for TRAP analysis. Consistent with our findings in mouse heteroplasmic cells (Fig.
374 2A), the formation of mature osteoclasts was significantly reduced in m.3243A>G cells (Fig. 6A).
375 Additionally, serum levels of the bone resorption marker CTX-1 were lower in m.3243A>G cells,
376 further indicating a systemic osteoclast deficiency (Fig. 6B). Next, we evaluated the effect of
377 spermidine in human cells on *in vitro* osteoclast differentiation in healthy and m.3243A>G cells
378 (Fig. 6C-D). Treatment with 5 µM spermidine increased the number of TRAP+ osteoclasts (Fig.
379 6C) and ATP levels (Fig. 6D) in both groups. To further explore the association between
380 m.3243A>G and bone mineral density (BMD) in humans, we analyzed data on 271,849
381 individuals from the UK Biobank cohort. Our study included individuals with BMD
382 measurements by ultrasound (n = 271,849) and Dual-energy X-ray Absorptiometry (DXA)
383 imaging (n = 46,777), along with whole genome sequencing data. Using whole genome
384 sequencing data, we identified 76 individuals with m.3243A>G at >5% blood heteroplasmy for
385 whom BMD data were available and 15 with DXA imaging (Supplementary Table 2). Linear
386 regression analysis, adjusted for relevant covariates, revealed no statistically significant
387 association between the presence of m.3243A>G and BMD measurements from heel, femoral
388 neck, spine (L1-L4), or total body (all p > 0.19) (Supplementary Table 3). Similarly, we found no
389 significant association with self-reported fractures (OR 0.528, p = 0.245) but confirmed a
390 known strong reported association with diabetes (OR 8.07, p = 8.22x10-15) (Supplementary
391 Table 4). A more sensitive analysis, limiting cases to those with >10% heteroplasmy, yielded
392 similar results (Supplementary Table 4). These results suggest that the blood levels of the
393 m.3243A>G variant may not significantly impact BMD or fracture risk in this population cohort.

394

395 ## Discussion

396 This work investigates how mitochondrial heteroplasmy disrupts OC differentiation by
397 impairing cellular metabolism and the proper assembly of the mtETC. Using a genetically
398 engineered mouse model, we showed that heteroplasmy prevents complex I subunit import
399 into mitochondria, leading to premature termination of osteoclastogenesis and reduced bone
400 resorption. We further demonstrate that spermidine can partially rescue OC function in both
401 heteroplasmic mice and heteroplasmic human cells carrying the m.3242A>G mutation. Our
402 findings highlight the crucial role of mtDNA in regulating OC differentiation, particularly under
403 challenging metabolic demands.

404 The metabolic requirements for OC differentiation and function are well studied. During OC
405 formation, glycolysis and glucose uptake via GLUT1 are increased, whereas the knockdown of
406 hypoxia inducible factor 1 alpha (Hif1a) or glucose deprivation inhibit OC function[45]. Specific
407 knockouts of respiratory complex I subunits result in deficiencies in OC maturation[10]. While
408 *Glut1*-mediated glucose metabolism through OXPHOS is critical for osteoclastogenesis, lactate
409 production from glucose is also necessary [46]. Hence, both glycolysis and oxidative
410 phosphorylation are required for OC formation. In fact, they may have two distinct key roles:
411 while oxidative phosphorylation appears to be the primary source for OC formation, glycolytic
412 pathway-related enzymes are distributed near the actin ring, where energy-demanding
413 activities associated with bone matrix degradation take place[4]. In conclusion, metabolic
414 dependencies differ between OC differentiation and active bone resorption: the formation of
415 OCs requires OXPHOS, while bone resorption is dependent on glycolysis[4,6]. In this study, we
416 examined how impaired osteoclast (OC) differentiation occurs when mitochondrial subunits
417 originate from different mitochondrial DNA variants. Our findings in heteroplasmic OC
418 precursors revealed increased complex I activity without a corresponding increase in ATP
419 production. This may be explained by dysfunction in downstream complexes, where electrons
420 donated by complex I are inefficiently transferred through the electron transport chain, leading
421 to an accumulation of electrons and reduced oxidative phosphorylation efficiency, ultimately
422 limiting ATP output. Elevated reactive oxygen species (ROS) levels or shifts in metabolic
423 pathways could further contribute to impaired ATP production.

424 The assembly of mitochondrial respiratory complex I in mammals requires the coordinated
425 integration of at least 44 subunits encoded by either nuclear and mitochondrial genomes[50].
426 The presence of complex I subcomplexes (intermediate state) in complex I-deficient cells (i.e.
427 when the complex is not assembled properly) indicates a sequential assembly process[51, 52 ,28].
428 This involves the complete import of nuclear-encoded subunits into mitochondria, degradation
429 of excess cytoplasmic material, and ultimately, the proper assembly and superassembly of
430 respiratory complex I in the mitochondrial lumen. Our data suggests that mitochondrial protein
431 subunits, in particular complex I, accumulate as unimported mitochondrial proteins in the
432 cytoplasm during osteoclast differentiation. Osteoclastogenesis is a tightly regulated process
433 that demands ATP not only for biomass generation but also for metabolic adaptation to
434 substrate availability at different stages. This process unfolds in a hypoxic tissue environment[47].
435 Intriguingly, hypoxia-induced mitochondrial stress granules have been identified in C. elegans[48].
436 Similarly during aerobic growth, yeast cells have been shown to accumulate mitochondrial
437 precursor proteins as MitoStores in the cytoplasm [49]. Hence, one explanation for complex I
438 being retained in the cytoplasm may be that this temporary storage site ensures their rapid
439 import into mitochondria during the later stages of differentiation, particularly under
440 challenging nutritional conditions or hypoxic induction. However, unassembled complex I
441 accumulate in the cytoplasm and are bound for degradation. Previous studies in mammalian
442 cells suggest that stress granules can be cleared either through an autophagy-independent
443 disassembly process or via autophagy-dependent degradation[53, 54]. The impaired autophagic

flux observed in the latter stages during OC differentiation in heteroplasmic BL/6$^{C57\text{-}NZB}$ cells may contribute to the cytoplasmic accumulation of complex I.

Mitochondrial heteroplasmy presents a largely unexplored area that may influence cellular function and bone health. Spermidine has been proposed to enhance autophagy[40,55], translational activity[37] and mitochondrial metabolism[42,56,57]. Collectively, these findings highlight spermidine as a promising candidate for improving mitochondrial quality. We and others have found that in both mice and humans a moiety of spermidine is needed to activate the translation factor eif5a by hypusination in order to increase autophagic flux and lysosomal activity[37,58]. Additionally, this translation factor is crucial for mitochondrial translation[41], and in T cells boosts oxidative metabolism by binding to the mitochondrial trifunctional protein (MTP)[42]. This implies that cellular spermidine levels may run low if this pathway is repeatedly triggered such as in heteroplasmy. Spermidine may need to be replenished or else an 'exhausted type' of autophagic flux occurs where LC3- II is no longer degraded, as we found here. We also observed that in wild-type cells spermidine inhibits OC differentiation. This is in line with the study that showed supplementation with spermine or spermidine enhances bone strength by inhibiting osteoclasts, whereas inhibiting polyamine biosynthesis reduces these benefits[43]. The differentiation of OC, like that of most cell types, requires autophagy and spermidine may help under homeostatic conditions. In contrast, in heteroplasmic mice, we found that spermidine enhanced OC differentiation at the dose that was previously reported to inhibit the process in wild-type cells[43]. Similar results have been observed in Nrf2 knockout cells[59], suggesting that spermidine levels may be critically low and need to be replenished under certain stressful situations such as excessive ROS, repeated clearance of either mitochondria or unwanted complexes I in the cytoplasm.

The association of bone density in people with the m.3243A>G mutation remains inconclusive. Several factors could explain this outcome. First, nuclear genetic variability, which influences osteoclast dysfunction, may act as a confounding factor. Our findings were based on inbred mouse strains, where genetic uniformity allowed clearer interpretation of mitochondrial effects, and maladaptive interactions are more easily detected. In mouse models, a mitochondrial-encoded protein can aberrantly interact with a nuclear-encoded protein from a different genetic background, leading to alterations on the function. In contrast, the genetically diverse human population introduces a wide range of nuclear genotypes and associated phenotypic variability, likely masking mitochondrial contributions and reducing the probability of detecting an association without very large sample sizes. The number of m.3243A>G carriers with bone measurements in the UK Biobank was very low, highlighting the need for larger studies to confirm or refute this null association. Future studies should further investigate these factors, including how nuclear genetic variation and osteoblast involvement contribute to bone phenotypes in the context of mitochondrial mutations in humans.

Our findings demonstrate that spermidine treatment can restore the assembly process and protein import leading to improved mitochondrial function in human *in vitro* OC differentiation, as well as *in vivo* in mice. The m.3243A>G mutation in people with MELAS and the

484 heteroplasmic BL/6$^{C57\text{-}NZB}$ mice are comparable in terms of their mitochondrial genetic
485 variability, each harboring two distinct mtDNA profiles and corresponding mitochondrial
486 function profiles. Comparing these two models allowed us to identify shared mechanisms
487 underlying mitochondria-related abnormalities of osteoclastogenesis and led to the discovery
488 of spermidine as a modulator of this process. This finding opens the door for the potential use
489 of spermidine in human heteroplasmic conditions, a therapeutic possibility not previously
490 reported.

491

492 Acknowledgements

493 We acknowledge all Autophagy in the Immune System group members for their scientific
494 discussions contributing to this manuscript and Prof. Jose Antonio Enríquez (Spanish National
495 Center for Cardiovascular Research, CNIC, Madrid) who provided mouse models for our
496 research and providing thoughtful feedback. We thank Dr. Hanlin Zhang from University of
497 California, Berkeley for discussions and constructive comments. We thank Jianwei Cui from the
498 University of Oxford who helped with experiments. We thank Patricia Cotta Moreira and Mino
499 Medghalchi from the Kennedy Institute of Rheumatology animal facility, and the Parc Cientific
500 de Barcelona (PCB) animal facility for their excellent care and assistance of animal well-being.
501 We thank Thomas Conrad, Caroline Braeuning and Sarah Nathalie Vitcetz at the MDC Genomics
502 Platform (BIH, Charité Campus Mitte, Berlin) for discussions about transcriptomic experiments
503 and sequencing performed at their facility. Histology was performed in the Kennedy Institute
504 of Rheumatology Histology Facility by Dr. Ida Parisi. We obtained confocal microscopy
505 assistance from Christoffer Lagerholm, Senior Advanced Microscopy Manager at the Kennedy
506 Institute of Rheumatology, and the Advanced Digital Microscopy (ADM) Core Facility at IRB
507 Barcelona is greatly appreciated. We thank the NHS Highly Specialised Service for Rare
508 Mitochondrial Disorders (Oxford University Hospitals, UK) for the patient recruitment and
509 share clinical samples. We thank Dr. Elisabeth Greßler from Max-Delbrück-Center for
510 Molecular Medicine and Hantao Lou from the University of Oxford for experimental assistance.
511 Images were created using BioRender.com under the academic license granted to AKS.

512

513 This work was supported by: University of Oxford Medical and Life Sciences Translational Fund
514 MC_PC_17174 and MC_PC_18059 from Wellcome ISSF fund to HL. China Scholarship Council
515 fund (202006320024) to JJ. UMDF PF-23-0010 to RJ-M. Biotechnology and Biological Sciences
516 Research Council (BBSRC, BB/X007049/1) to SM. Kennedy Trust Prize Studentship (AZT00050-
517 AZ04) to JZ. Chinese Academy of Medical Sciences (CAMS) Innovation Fund for Medical
518 Sciences (CIFMS) 2018-I2M-2-002 to LL. Centre for OA Pathogenesis (Versus Arthritis 20205)
519 to TLV. KTRR KENN202111 to AW. Oxford Hospitals charity and Lily Foundation "Treatments
520 for Mitochondrial Disease – 2019/20" to JP. Salary support from the UK NHS Specialist
521 Commissioners who fund the "Rare Mitochondrial Disorders of Adults and Children" clinical
522 Service to SDW. Novo Nordisk Foundation (NNF0064142) to COC. This work is funded by
523 Diabetes UK (19/0005994 and 21/0006335), MRC (MR/T00200X/1) and Wellcome's
524 Institutional Strategic Support Fund awarded to University of Exeter; KAP and TH is funded by

Wellcome (219606/Z/19/Z); The work is supported by the National Institute for Health Research (NIHR) Exeter Biomedical Research Centre, Exeter, UK. European Molecular Biology Organization Postdoctoral Fellowship (EMBO) ALTF115-2019, “La Caixa” Foundation (ID 100010434, LCF/BQ/PI24/12040005) and funding from MINECO through the Centres of Excellence Severo Ochoa Award and CERCA Programme of the Generalitat de Catalunya to AVL-V. Wellcome Trust Fund 220784/Z/20/Z to AKS.

Author contributions

AKS, A.V.L.-V. and H.L. conceptualized and designed the study.
A.V.L.-V., H.L., and J.J. performed and analyzed experiments, methodology, and investigation.
AKS, A.V.L.-V., H.L. and J.J. discussed analyses.
AKS and A.V.L.-V. supervised the project and interpreted the experimental data.
AKS, A.V.L.-V., H.L. and J.J. wrote the original draft.
AKS, A.V.L.-V., H.L., J.J. and TLV reviewed and edited the manuscript.
C.OC. planned experiments, analyzed data and edited the final manuscript.
K.G. performed mitochondrial DNA copy numbers, respiratory complexes activities and confocal imaging.
R.J-M. performed respiratory complexes analyses.
T.H. and K.A.P. investigated the association between m.3243A>G and bone parameters in individuals from the UK Biobank cohort.
J.Z. and TLV contributed to the 3D reconstructions of bone images and image analysis.
L.L. performed the isolation of donor PBMC samples, followed by OC differentiation, and autophagy flux assays.
S.W. and A.W. analyzed the bone stiffness parameters.
S.D.W. and J.P. provided samples and contributed to discussions on human and patient data.
All authors reviewed and approved the final manuscript.

Competing interests

The authors declare no competing interests.

Limitations of the study

The inconclusive findings regarding bone density in m.3243A>G patients may be influenced by several factors, including population heterogeneity across the non-mitochondrial genome, the complex interplay between osteoblast function and nuclear variability in ameliorating OC dysfunction, potentially affecting the overall bone phenotype. The number of m.3243A>G carriers in our bone phenotypic analysis were low, and large studies are needed to replicate this null association. Additionally, our study used inbred mouse strains, which may limit the generalizability of our findings to a broader, genetically diverse human population. Future studies should investigate these factors further, examining how nuclear genetic variation and osteoblast involvement contribute to the observed outcomes.

References

1. Leng, H. *et al.* Modulating glycosphingolipid metabolism and autophagy improves outcomes in pre-clinical models of myeloma bone disease. *Nat. Commun.* **13**, 7868 (2022).
2. Tao, X. *et al.* Clinical Characteristics and Pathogenic Gene Identification in Chinese Patients With Paget's Disease of Bone. *Front. Endocrinol.* **13**, 850462 (2022).
3. Ledesma-Colunga, M. G., Passin, V., Lademann, F., Hofbauer, L. C. & Rauner, M. Novel Insights into Osteoclast Energy Metabolism. *Curr. Osteoporos. Rep.* **21**, 660–669 (2023).
4. Lemma, S. *et al.* Energy metabolism in osteoclast formation and activity. *Int. J. Biochem. Cell Biol.* **79**, 168–180 (2016).
5. Taubmann, J. *et al.* Metabolic reprogramming of osteoclasts represents a therapeutic target during the treatment of osteoporosis. *Sci. Rep.* **10**, 21020 (2020).
6. Jiménez, J. A., Lawlor, E. R. & Lyssiotis, C. A. Amino acid metabolism in primary bone sarcomas. *Front. Oncol.* **12**, 1001318 (2022).
7. Motyl, K. J., Guntur, A. R., Carvalho, A. L. & Rosen, C. J. Energy Metabolism of Bone. *Toxicol. Pathol.* **45**, 887–893 (2017).
8. Zeng, R., Faccio, R. & Novack, D. V. Alternative NF-κB Regulates RANKL-Induced Osteoclast Differentiation and Mitochondrial Biogenesis via Independent Mechanisms. *J. Bone Miner. Res.* **30**, 2287–2299 (2015).
9. Marques-Carvalho, A., Sardão, V. A., Kim, H.-N. & Almeida, M. ECSIT is essential for RANKL-induced stimulation of mitochondria in osteoclasts and a target for the anti-osteoclastogenic effects of estrogens. *Front. Endocrinol.* **14**, 1110369 (2023).

591 10. Jin, Z., Wei, W., Yang, M., Du, Y. & Wan, Y. Mitochondrial Complex I Activity Suppresses
592 Inflammation and Enhances Bone Resorption by Shifting Macrophage-Osteoclast
593 Polarization. *Cell Metab.* **20**, 483–498 (2014).
594 11. Naue, J. *et al.* Evidence for frequent and tissue-specific sequence heteroplasmy in
595 human mitochondrial DNA. *Mitochondrion* **20**, 82–94 (2015).
596 12. Goto, Y., Nonaka, I. & Horai, S. A mutation in the tRNALeu(UUR) gene associated with
597 the MELAS subgroup of mitochondrial encephalomyopathies. *Nature* **348**, 651–653
598 (1990).
599 13. Hirano, M. *et al.* MELAS: An original case and clinical criteria for diagnosis. *Neuromuscul.*
600 *Disord.* **2**, 125–135 (1992).
601 14. Ng, Y. S. & Gorman, G. S. Stroke-like episodes in adult mitochondrial disease. in
602 *Handbook of Clinical Neurology* vol. 194 65–78 (Elsevier, 2023).
603 15. Gandhi, S. S., Muraresku, C., McCormick, E. M., Falk, M. J. & McCormack, S. E. Risk
604 factors for poor bone health in primary mitochondrial disease. *J. Inherit. Metab. Dis.* **40**,
605 673–683 (2017).
606 16. Di Stadio, A. *et al.* Hearing impairment in MELAS: new prospective in clinical use of
607 microRNA, a systematic review. *Orphanet J. Rare Dis.* **13**, 35 (2018).
608 17. Handzel, O., Ungar, O. J., Lee, D. J. & Nadol, J. B. Temporal bone histopathology in
609 MELAS syndrome. *Laryngoscope Investig. Otolaryngol.* **5**, 152–156 (2020).
610 18. Fu, Y. *et al.* Engineering mtDNA deletions by reconstituting end joining in human
611 mitochondria. *Cell* S0092867425001941 (2025) doi:10.1016/j.cell.2025.02.009.
612 19. Latorre-Pellicer, A. *et al.* Mitochondrial and nuclear DNA matching shapes metabolism
613 and healthy ageing. *Nature* **535**, 561–565 (2016).

614 20. Lechuga-Vieco, A. V. *et al.* Cell identity and nucleo-mitochondrial genetic context
615 modulate OXPHOS performance and determine somatic heteroplasmy dynamics. *Sci.*
616 *Adv.* **6**, eaba5345 (2020).
617 21. Bergen, V., Lange, M., Peidli, S., Wolf, F. A. & Theis, F. J. Generalizing RNA velocity to
618 transient cell states through dynamical modeling. *Nat. Biotechnol.* **38**, 1408–1414
619 (2020).
620 22. Lange, M. *et al.* CellRank for directed single-cell fate mapping. *Nat. Methods* **19**, 159–
621 170 (2022).
622 23. Dann, E., Henderson, N. C., Teichmann, S. A., Morgan, M. D. & Marioni, J. C. Differential
623 abundance testing on single-cell data using k-nearest neighbor graphs. *Nat. Biotechnol.*
624 **40**, 245–253 (2022).
625 24. Tsukasaki, M. *et al.* Stepwise cell fate decision pathways during osteoclastogenesis at
626 single-cell resolution. *Nat. Metab.* **2**, 1382–1390 (2020).
627 25. Indo, Y. *et al.* Metabolic regulation of osteoclast differentiation and function. *J. Bone*
628 *Miner. Res. Off. J. Am. Soc. Bone Miner. Res.* **28**, 2392–2399 (2013).
629 26. Zieliński, Ł. P., Smith, A. C., Smith, A. G. & Robinson, A. J. Metabolic flexibility of
630 mitochondrial respiratory chain disorders predicted by computer modelling.
631 *Mitochondrion* **31**, 45–55 (2016).
632 27. Wachter, C., Schatz, G. & Glick, B. S. Protein import into mitochondria: the requirement
633 for external ATP is precursor-specific whereas intramitochondrial ATP is universally
634 needed for translocation into the matrix. *Mol. Biol. Cell* **5**, 465–474 (1994).
635 28. Lazarou, M., McKenzie, M., Ohtake, A., Thorburn, D. R. & Ryan, M. T. Analysis of the
636 assembly profiles for mitochondrial- and nuclear-DNA-encoded subunits into complex I.
637 *Mol. Cell. Biol.* **27**, 4228–4237 (2007).

638 29. Franco-Iborra, S. *et al.* Defective mitochondrial protein import contributes to complex I-
639 induced mitochondrial dysfunction and neurodegeneration in Parkinson's disease. *Cell*
640 *Death Dis.* **9**, 1122 (2018).
641 30. Thomas, H. E. *et al.* Mitochondrial Complex I Activity Is Required for Maximal
642 Autophagy. *Cell Rep.* **24**, 2404-2417.e8 (2018).
643 31. Kulawiak, B. *et al.* The mitochondrial protein import machinery has multiple connections
644 to the respiratory chain. *Biochim. Biophys. Acta BBA - Bioenerg.* **1827**, 612–626 (2013).
645 32. Park-Min, K.-H. Metabolic reprogramming in osteoclasts. *Semin. Immunopathol.* **41**,
646 565–572 (2019).
647 33. Lareau, C. A. *et al.* Massively parallel single-cell mitochondrial DNA genotyping and
648 chromatin profiling. *Nat. Biotechnol.* **39**, 451–461 (2021).
649 34. Latorre-Pellicer, A. *et al.* Regulation of Mother-to-Offspring Transmission of mtDNA
650 Heteroplasmy. *Cell Metab.* **30**, 1120-1130.e5 (2019).
651 35. Burgstaller, J. P. *et al.* MtDNA segregation in heteroplasmic tissues is common in vivo
652 and modulated by haplotype differences and developmental stage. *Cell Rep.* **7**, 2031–
653 2041 (2014).
654 36. Johnston, I. G. & Jones, N. S. Evolution of Cell-to-Cell Variability in Stochastic, Controlled,
655 Heteroplasmic mtDNA Populations. *Am. J. Hum. Genet.* **99**, 1150–1162 (2016).
656 37. Zhang, H. *et al.* Polyamines Control eIF5A Hypusination, TFEB Translation, and
657 Autophagy to Reverse B Cell Senescence. *Mol. Cell* **76**, 110-125.e9 (2019).
658 38. Calabrese, C. *et al.* Mitochondrial translocation of TFEB regulates complex I and
659 inflammation. *EMBO Rep.* **25**, 704–724 (2024).
660 39. Alsaleh, G. *et al.* Autophagy in T cells from aged donors is maintained by spermidine and
661 correlates with function and vaccine responses. *eLife* **9**, e57950 (2020).

662 40. Puleston, D. J. *et al.* Autophagy is a critical regulator of memory CD8+ T cell formation.
663 *eLife* **3**, e03706 (2014).
664 41. Puleston, D. J. *et al.* Polyamines and eIF5A Hypusination Modulate Mitochondrial
665 Respiration and Macrophage Activation. *Cell Metab.* **30**, 352-363.e8 (2019).
666 42. Al-Habsi, M. *et al.* Spermidine activates mitochondrial trifunctional protein and
667 improves antitumor immunity in mice. *Science* **378**, eabj3510 (2022).
668 43. Chevalier, C. *et al.* Warmth Prevents Bone Loss Through the Gut Microbiota. *Cell Metab.*
669 **32**, 575-590.e7 (2020).
670 44. Langdahl, J. H. *et al.* Mitochondrial Point Mutation m.3243A>G Associates With Lower
671 Bone Mineral Density, Thinner Cortices, and Reduced Bone Strength: A Case-Control
672 Study. *J. Bone Miner. Res. Off. J. Am. Soc. Bone Miner. Res.* **32**, 2041–2048 (2017).
673 45. Indo, Y. *et al.* Metabolic regulation of osteoclast differentiation and function. *J. Bone*
674 *Miner. Res. Off. J. Am. Soc. Bone Miner. Res.* **28**, 2392–2399 (2013).
675 46. Li, B. *et al.* Both aerobic glycolysis and mitochondrial respiration are required for
676 osteoclast differentiation. *FASEB J. Off. Publ. Fed. Am. Soc. Exp. Biol.* **34**, 11058–11067
677 (2020).
678 47. Zhou, P., Zheng, T. & Zhao, B. Cytokine-mediated immunomodulation of
679 osteoclastogenesis. *Bone* **164**, 116540 (2022).
680 48. Sun, C.-L., Van Gilst, M. & Crowder, C. M. Hypoxia-induced mitochondrial stress
681 granules. *Cell Death Dis.* **14**, 448 (2023).
682 49. Krämer, L. *et al.* MitoStores: chaperone-controlled protein granules store mitochondrial
683 precursors in the cytosol. *EMBO J.* **42**, e112309 (2023).

684 50. Formosa, L. E., Dibley, M. G., Stroud, D. A. & Ryan, M. T. Building a complex complex:
685 Assembly of mitochondrial respiratory chain complex I. *Semin. Cell Dev. Biol.* **76**, 154–
686 162 (2018).
687 51. Guerrero-Castillo, S. *et al.* The Assembly Pathway of Mitochondrial Respiratory Chain
688 Complex I. *Cell Metab.* **25**, 128–139 (2017).
689 52. Hoefs, S. J. G. *et al.* Novel mutations in the NDUFS1 gene cause low residual activities in
690 human complex I deficiencies. *Mol. Genet. Metab.* **100**, 251–256 (2010).
691 53. Buchan, J. R., Kolaitis, R.-M., Taylor, J. P. & Parker, R. Eukaryotic stress granules are
692 cleared by autophagy and Cdc48/VCP function. *Cell* **153**, 1461–1474 (2013).
693 54. Gwon, Y. *et al.* Ubiquitination of G3BP1 mediates stress granule disassembly in a
694 context-specific manner. *Science* **372**, eabf6548 (2021).
695 55. Hofer, S. J. *et al.* Spermidine is essential for fasting-mediated autophagy and longevity.
696 *Nat. Cell Biol.* **26**, 1571–1584 (2024).
697 56. Zhou, J. *et al.* Spermidine-mediated hypusination of translation factor EIF5A improves
698 mitochondrial fatty acid oxidation and prevents non-alcoholic steatohepatitis
699 progression. *Nat. Commun.* **13**, 5202 (2022).
700 57. Messerer, J. *et al.* Spermidine supplementation influences mitochondrial number and
701 morphology in the heart of aged mice. *J. Anat.* **242**, 91–101 (2023).
702 58. Rossi, D., Kuroshu, R., Zanelli, C. F. & Valentini, S. R. eIF5A and EF -P: two unique
703 translation factors are now traveling the same road. *WIREs RNA* **5**, 209–222 (2014).
704 59. Dong, Y. *et al.* A clinical-stage Nrf2 activator suppresses osteoclast differentiation via the
705 iron-ornithine axis. *Cell Metab.* **36**, 1679-1695.e6 (2024).
706

Materials and methods

Lead Contact and Materials Availability

Further information and requests for resources and reagents should be directed to and will be fulfilled by the Lead Contacts, Anna Katharina Simon (katja.simon@kennedy.ox.ac.uk) and Ana Victoria Lechuga-Vieco (ana.lechugavieco@irbbarcelona.org).

Materials availability

Animal lines generated in this study will be made available on request, but we may require a payment and/or a completed Materials Transfer Agreement if there is potential for commercial application.

Data and code availability

All data reported in this paper will be shared by the lead contact upon request. Original sequencing data files have been deposited at NCBI-SRA (PRJNA1144799), with a temporary link to access the metadata (https://dataview.ncbi.nlm.nih.gov/object/PRJNA1144799?reviewer=45rhoehhhq1rkj66o92nrv2pds). Links or accession numbers are also listed in the key resources table. The datasets will be publicly available upon the publication of this manuscript. This paper does report original code. The code for 3D bone shape reconstruction/evaluation and OC/OB quantification for in-vitro staining (Supplementary Table 1) can be found in GitHub repository: https://github.com/jianqingzheng/image_processing. Any additional information required to reanalyze the data reported in this work paper is available from the lead contact upon request.

Experimental model and subject details

Animals

All animal experiments were done in compliance with the guidelines established by the UK Animal (Scientific Procedures) Act 1986 and the Institutional Animal Care and Use Committee of the Barcelona Science Park and University of Barcelona. In vivo experiments with animals were undertaken under the UK Home Office Project License PPL 30/3388. Unless otherwise specified, all experiments were performed in 8- to 12-week-old mice in a C57BL/6JOlaHsd background and and a heteroplasmic mouse strain with the nuclear genome of C57BL/6JOlaHsd but mitochondrial DNA of C57+NZB (referred to as BL/6$^{C57\text{-}NZB}$)[1]. Mice were housed in specific pathogen-free facilities at the Kennedy Institue of Rheumatology (NDORMS, University of Oxford) and Park Scientific of Barcelona (PCB) under a 12-hour light/dark cycle and had ad libitum access to water and a standard chow diet (SDS diets 801,151; 75% energy from carbohydrates, 17.5% from protein, and 7.5% from fat).

Patient samples

Patient blood samples were obtained with the approval of the United Kingdom National Research Ethics Service (South Central-Berkshire, approval number 20/04, IRAS 162181). Written informed consent was obtained from all participants, and all procedures were carried out in accordance with relevant national and international guidelines and regulations. This research has been conducted using the UK Biobank Resource. This work was carried out under UK Biobank project number 103356.

Methods details

Micro computed tomography (µCT) scan and analysis of bone structure

The PerkinElmer QuantumFX scanner was utilized to scan the tibiae. The region of interest was specified as 100 slices below the growth plate of the proximal tibia and scanned for 3 minutes with an energy of 90KV, 200uA, and

field of view of 10. The resulting bone data from the scan were subjected to analysis through the use of Analyse-12.0 software and Analyse-14.0 software.

Compression testing of femur

After being harvested, the femurs were stored directly in -20°C. To prepare for the compression test, the femurs were rehydrated with PBS at 4°C overnight. Murine right femurs were subjected to compression test using Electroforce 5500 (TA Instruments, Germany) on a 200 N load. Bones were secured on the lower plate and compressed. For testing, the bones were pre-loaded with a contact force of -0.5 N and load-displacement curves were generated in displacement control at a cross-head speed of 0.3 mm/s until failure of the diaphyseal region. Ultimate load was recorded for each group as an indicator of bone strength.

Serum and BM tissue processing

On the day of sacrifice, intracardiac puncture was used to collect mouse blood samples using capillary blood collection tubes (16.440, Microvette® CB 300 Z). The collected blood samples were kept on ice for up to 2 hours and then centrifuged at full speed for 5 minutes to extract the serum (supernatant). Serum was stored at −80°C until further analysis. To collect mouse BM cells, the femurs were crushed with a mortar and pestle in PBS-0.1% BSA-2 mM EDTA. The mixture was then filtered through 70µm cell strainers, and the collected cells were stored on ice, ready for flow cytometry without RBC lysis.

ELISA (Enzyme-Linked Immunosorbent Assay)

Mouse serum CTX1 level, mouse serum P1NP level and human serum CTX1 level were measured by ELISA according to the manufacturer's instructions.

Tartrate-Resistant Acid Phosphatase (TRAP) Staining

TRAP staining and counterstained with 0.2% methyl green solution experiments were previously described[2] and conducted according to the manufacturer's instructions. TRAP positive multi-nuclear (>3 nuclei) OC were counted. The Zeiss AxioScan Z1 Slide Scanner at the Wolfson Imaging Centre, WIMM, University of Oxford was used to acquire the images of OC.

TRAP staining and histomorphometry analysis of tibiae

Tibiae were fixed in 4% PFA at 4°C overnight and then decalcified in 10% Ethylenediaminetetraacetic acid (EDTA) decalcification solution for a duration of 14 days (buffer changed every 3 days). After decalcification, the tibiae were paraffin embedded for sectioning using a Leica RM2235 microtome, resulting in sections of 5µm thickness to create histology slides (VWR 631-1553). The sections were processed and stained with TRAP solution, followed by counterstaining with 0.2% methyl green solution. Histology slides were scanned using the Hamamatsu NanoZoomer S210 (WIMM, the University of Oxford). OC parameters from histology slides were manually quantified by a researcher from JingLianWen Technology (https://www.jinglianwen.com) blinded to the mouse experiment groups.

Bone Marrow Transplant and chimera blood lineages analysis

To establish BM chimeras, 8-12-week-old female BL/6$^{C57\text{-}NZB}$ mice and CD45.1^{+} B6.SJL female mice were lethally irradiated at the dose of 11 Gy (550 cGy twice, 4 hours apart) and rested for 1 hour prior to injection. 1.5 million BM cells derived from 8-12-week-old BL/6$^{C57\text{-}NZB}$ and BL/6^{C57} female mice or their respective littermates were transplanted (i.v. injection) into these irradiated mice. Reconstitution effectiveness was evaluated by analysing the percentage of CD45.1^{+}, CD45.2^{+} and CD45.1/2^{+} cells in the blood PBMCs of bone marrow-transplanted mice at 2,4, 6 and 8 weeks post-irradiation. To achieve this, we collected 50 microliters of blood from tail vein bleeding and treated it with RBC Lysis Buffer for 5 minutes. After centrifugation, the supernatant was removed, and the cells were stained with antibodies for flow cytometry analysis. Given that previous research[3] demonstrated that three weeks is sufficient for OC replenishment after transplantation, mice were sacrificed 8-9 weeks following lethal irradiation and transplantation.

This ensured comprehensive reconstitution of most cell lineages with the transplanted cells. Both blood and bone samples were collected for further analysis.

Mouse In vitro OC differentiation

Mouse in vitro OC differentiation method was previously described[2]. In brief, 8-week-old mouse BM cells were treated with 50 ng/ml M-CSF in Alpha-MEM culture media with 10% FBS, 1% pen/strep, and 1% L-glutamine for 48 hours (day -2) in 96-well plates. On day 0, the adherent cells were differentiated into OCs with 10 ng/ml mouse M-CSF and 50 ng/ml mouse RANKL. Spermidine was added at the dosage of 10uM. Culture media was refreshed every 3 days and OCs were identified by TRAP staining on day 5. The Olympus BX51 microscope at the Kennedy Institute of Rheumatology and AID ELISpot Reader System (ELR078IFL, AID GmbH) at the Wellcome Centre for Human Genetics were used to acquire the images of OC.

Flow Cytometry

Bone marrow and blood samples were collected from mice and prepared for flow cytometry. Erythrocytes were lysed using eBioscience™ 1X RBC Lysis Buffer. Cells were first incubated with FcR blocker in PBS for 20 minutes, followed by incubation with surface-conjugated antibodies for 30 minutes at 4°C. Conjugated antibodies used for surface staining were: anti-CD45.1, anti-CD45.2, anti- CD45R, anti-CD3e, anti-CD11b, anti-CD117 and anti-CD115. Identification of viable cells was done by fixable Zombie Aqua Live/Dead or near-IR dead cell staining. Stained samples were fixed with BD Cytofix™ Fixation Buffer for 15 minutes at RT. All samples were washed and stored in PBS containing 5 mM EDTA (Sigma-Aldrich) and 2% FBS (Sigma-Aldrich) before acquisition. To determine the absolute cell count within tissues, 10,000 or 20,000 CountBright™ absolute counting beads were added to each sample before flow cytometry to determine the total cell count per bone or blood volume. To ensure accuracy, over 2,000 beads were acquired per tube. Samples were acquired on a FACS LSR II (R/B/V) or Fortessa X20 (R/B/V/YG) flow cytometer (BD Biosciences) using FACSDiva software and analysed with FlowJo (version 10.10, BD Biosciences).

Mitochondrial content and ROS levels during OC differentiation: Mitochondrial content and ROS levels were assessed using Nonyl acridine orange (NAO) and CellROX™ Deep Red dyes. Cells were collected and incubated with 100 nM NAO and 5 µM CellROX™ for 20 minutes at 37°C. Ex/Em: 450/530 nm for NAO and 644/665 nm for CellROX™. After washing, cells were surface-stained and prepared for flow cytometry analysis as described in the previous section.

Autophagy flux (Flow cytometry). Autophagy levels were assessed as previously described[4]. In brief, cells were treated for 2 hours with either bafilomycin A1 (10 nM BafA1) or vehicle control, followed by staining using the FlowCellect™ Autophagy LC3 Antibody-based assay kit. After labeling with surface markers (as described earlier), cells were washed with Assay Buffer in 96-well U-bottom plates. Permeabilization was performed with 0.05% saponin, followed by immediate centrifugation. Cells were then incubated with anti-LC3 (FITC) at 1:20 dilution in Assay Buffer for 30 minutes at 4°C, followed by a final wash with 150 µL Assay Buffer. Autophagic flux was determined by calculating the LC3-II median fluorescence intensity as (BafA1 - Vehicle) / Vehicle.

Pre-processing of single-cell RNA-seq data

To collect mouse BM cells, the femurs were crushed with a mortar and pestle in PBS-0.1% BSA-2 mM EDTA. The mixture was then filtered through 70µm cell strainers, and the collected cells were plated for in vitro OC differentiation with 50 ng/ml M-CSF in Alpha-MEM culture media. On day 0, the adherent cells were differentiated into OCs with 10 ng/ml mouse M-CSF and 50 ng/ml mouse RANKL. Cells were harvested at the specified time points and were labeled with Cell Multiplexing Oligos (10x Genomics) according to the manufacturer's instructions. Barcoded sequencing libraries of multiplexed single-cell samples were generated using 10X Genomics Chromium system with 3' chemistry. Due to a technique issue, two of the three biological replicates were pooled together prior to the multiplexing step and were treated as single replicate (rep2) in the downstream analysis.

Computational analysis of single-cell RNA-seq data

Raw gene counts were normalized by sequencing depth and log1p transformed in Seurat. Batch effects were corrected using harmony[5] with n=10,000 variable features, while each sample was treated as an individual batch. Cells were then integrated using n = 30 harmony-corrected principal components, clustered at the resolution of 0.5 and then projected in 2D space using uniform manifold approximation and projection (UMAP). Any clusters that belonged to a non-myeloid lineage or had abnormally high levels of nuclear transcripts (possibly damaged cells with intact nuclei) were discarded, leaving n=10,809 cells for downstream analyses. Cluster marker genes and differentially expressed genes between mouse groups were identified by the Wilcoxon rank-sum test implemented in the Seurat package, and p-values were adjusted using the Benjamini-Hochberg procedure. Pathway enrichment was performed using XGR[6]. Genes associated with oxidative phosphorylation (OXPHOS) were obtained from the KEGG database and were converted to mouse symbols using Ensembl genome database. OXPHOS scores were computed using the "AddModuleScore" function in Seurat, and normalized against a set of n=100 random control genes.

The trajectory of osteoclast differentiation was recovered using information from RNA velocity. In brief, genes with a minimum of 20 spliced and 20 unspliced transcripts were extracted from the Cell Ranger alignment outputs and were analyzed in scVelo[7]. The splicing kinetics were recovered using the dynamical model and n=500 top velocity genes. For consistency, we used the same nearest-neighbor graph constructed from scRNA-seq data for all velocity analysis, and inferred velocities were projected onto the scRNA-seq UMAP. The initial and terminal clusters of the differentiation trajectory, together with a latent time for each cell, were inferred using CellRank[8]. We used the default combination of a velocity kernel (80%, deterministic mode) and a connectivity kernel (20%, computed based on the nearest-neighbor graph) to compute the probabilities for cell-cell transitions. The cell-level transitional probabilities were then aggregated at a cluster level and plotted as a fate map using directed PAGA[9].

For differential abundance test between BL/6^{C57}, and BL/6$^{C57\text{-}NZB}$ samples, batch-corrected principal components were used to construct single-cell neighborhoods using Milo[10], with prop = 0.1, k=20 and d=30. In brief, cells from BL/6^{C57} or BL/6$^{C57\text{-}NZB}$ samples were counted within each neighborhood, and the statistical significance of differential abundance was evaluated using a generalized linear model with biological replicates included as covariates. The test results were visualized on a UMAP using the "plotNhoodGraphDA" function.

Mitochondrial genotyping using single-cell RNA-seq data

Genetic variants in mitochondrial transcripts were recovered at single-cell level using the mgatk pipeline[11]. In brief, sequencing reads were first aligned to a hard-masked mm10 reference genome using CellRanger (v7.1.0; 10x Genomics), followed by mgatk execution to compute the per variant coverage across the mitochondrial genome. The per-cell heteroplasmic ratio was calculated by dividing the summed allelic coverage of all variants specific to NZB mitochondria (n=90, Supplementary Table 1) over the total sequencing coverage at these locations. Only BL/6$^{C57\text{-}NZB}$ cells with more than 10 reads covering these variants were retained (n=3,093) for downstream analyses.

Seahorse analyses

Metabolic assays were performed using a Seahorse XFe96 Analyzer with Seahorse XF Cell Mito Stress Test Kit according to the manufacturer's instructions. Day 0, Day 1 and Day 3 pre-OCs were seeded in a 96-well plate at the density of 25,000, 25,000and 15,000 cells per well. Cells were treated with 10 ng/ml mouse M-CSF and 50 ng/ml mouse RANKL for indicated time prior to the assay. A final concentration of 1 uM oligomycin, 2 uM FCCP and 1 uM Rotenone and Antimycin A was used based on a pilot titration experiment. Cell density was quantified by CyQuant staining post Seahorse for data normalization.

ATP Synthesis

ATP levels were quantified using the ATP Bioluminescence Assay Kit CLS II following the manufacturer's protocol. Briefly, equal numbers of cells from each condition were pelleted, boiled in Tris-EDTA buffer (pH 7.74) for 2 minutes, centrifuged, and the supernatant was analyzed. Luminescence was measured in a CLARIOstar plate reader (BMG LABTECH).

Analysis of Complex I and Complex II Respiratory Activities

Enzymatic activities were measured spectrophotometrically using the Beer-Lambert law as previously described[12]. Briefly, assays were conducted at 32°C with frozen-thawed mitochondria in activity buffers. Complex I activity was initiated with 130 µM NADH and monitored at 340 nm, subtracting rotenone-insensitive rates. NADH:O_2 and NADH:decylubiquinone activities were assessed in sucrose buffer with specific inhibitors. Complex II activity was measured at 600 nm after adding 10 mM succinate.

Western Blot Analyses

Autophagy flux during OC differentiation was assessed by incubating the cells in culture media supplemented with 10nM Bafilomycin A1 for 2 h, with DMSO served as the vehicle control. Autophagic flux was calculated as the ratio of LC3-I to LC3-II.

Cell lysis was performed on ice using NP-40 lysis buffer containing proteinase inhibitors and Phosphatase Inhibitor Cocktail 2. Afterward, the protein concentration was determined using the Pierce™ BCA Protein Assay Kits. The lysate was then treated with Reducing Laemmli Sample Buffer and 15–30 µg of proteins were loaded onto SDS-PAGE gels. For the separation of LC3-I and LC3-II, a 15% Tris-HCl gel and SDS running buffer were employed, while NuPAGE Novex 4–12% Bis-Tris gradient gels with NuPAGE™ MES SDS Running Buffer (1X) were used for other proteins. Proteins were subsequently transferred to a PVDF membrane and blocked with 5% skimmed milk-PBST. Primary antibodies were incubated overnight in 1% milk, followed by secondary antibody incubation in 1% milk with 0.01% SDS for 1 hour. The following primary antibodies were used: anti-LC3, anti-p62, anti-bActin and Total OXPHOS Rodent WB Antibody Cocktail. Imaging was performed using the Odyssey CLx Imaging System, capturing the signals from IRDye 800CW Donkey Anti-Rabbit IgG (H+L) (1:10,000 dilution) and IRDye 680RD Donkey Anti-Mouse IgG (H+L) (1:10,000 dilution) simultaneously, with varying intensities based on fluorescent exposure. See the Key resources table for a list of primary and secondary antibodies. Data analysis was carried out using Image Studio Lite.

Confocal imaging

Bone marrow cells were seeded with 10 ng/ml mouse M-CSF and 50 ng/ml mouse RANKL and differentiated for 1, 3, and 5 days in µ-Slide 18 Well Ibidi chamber slides (81816, Ibidi GmbH). Cells were fixed with 4% paraformaldehyde for 10mins and permeabilized with 0.2% Triton X-100 in PBS for another 10min in room temperature. Cells were blocked with PBS containing 2% BSA and 0.01% Tween20 for 1h and incubated with the primary antibodies overnight at 4°C. The following antibodies were used to perform immunofluorescence staining in murine and human cells: mouse anti-NDUFA9 (20C11B11B11), anti-NDUFB7 (Polyclonal), anti-ATPB (3D5), anti-TOMM20 (EPR15581-54). After washing with PBS for three times, cells were incubated in 2% BSA-PBS for 1 hour with the following secondary antibodies: anti-mouse IgG AF488, anti-mouse AF647, anti-mouse AF546, anti-rabbit AF488 and anti-rabbit AF568. After washing with PBS and stained with 2ug/ml DAPI for 10mins, coverslips were mounted in SlowFade™ Diamond Antifade Mountant. Forty to eighty Z-stacks (0.13 µm) were acquired using a Zeiss LSM 980 Airyscan2 confocal system and the ZenBlue software. Data were analysed using ImageJ/Fiji[14].

Genotyping and Heteroplasmy Analysis

Heteroplasmy levels were assessed as previously described[15].H Briefly, mice were genotyped at postnatal day 21 using DNA extracted from ear notches with the REDExtract-N-Amp™ Tissue PCR Kit. Additionally, DNA from cells undergoing OC differentiation (Day 0, Day 1, Day 3, and Day 5) was isolated using 50 mM NaOH at 95°C, followed by neutralization with Tris-HCl (pH 7.5). The G4276A polymorphism, which introduces a BamHI restriction site in C57 mtDNA but not in NZB mtDNA, was used for genotyping. DNA was PCR-amplified with REDExtract-N-Amp™ PCR ReadyMix using primers: Forward 5′-AAGCTATCGGGCCCATACCCCG-3′ (3862-3884) and Reverse 5′-GTTGAGTAGAGTGAGGGATGGG-3′ (4503-4525), under the following conditions: 95° C (30s), 58° C (30s), 72°

C (45s) for 30 cycles. The PCR product was digested with FastDigest BamHI at 37° C for 20 minutes and analysed via agarose gel electrophoresis. DNA bands were visualised using the Gel Doc XR+ System (Bio-Rad) and quantified with Quantity One Software. The NZB mtDNA proportion was determined by the ratio of undigested 664-bp fragments to the total of 664-bp (undigested) and 414/250-bp (digested) fragments, with heteroduplex formation corrected using a standard curve from mixed C57 and NZB mtDNA samples.

Mitochondrial DNA copy number

Total DNA from cells undergoing osteoclast differentiation (Day 0, Day 1, Day 3, and Day 5) was isolated using 50 mM NaOH at 95°C, followed by neutralization with Tris-HCl (pH 7.5). qRT-PCR was performed on Applied Biosystems ®ViiA ™7 Real-Time PCR System using Power SYBR™ Green Master Mix in a 96-well plate to quantify mtDNA copy number relative to nDNA. The primers used were mtCo2 (mtDNA): COII RTF (3'-CTACAAGACGCCACAT-5', 7037-7052) and COII RTR (3'-GAGGGGGAGAGCAAT-5', 7253-7238), and SDH (nDNA): SDH RTF (3'-TACTACAGCCCCAAGTCT-5', 1026-1043) and SDH RTR (3'-TGGACCCATCTTCTATGC-5', 1219-1202). PCR conditions included an initial denaturation at 95ºC for 2 min, followed by 40 cycles of 95ºC for 15 s and 60ºC for 60 s, with a dissociation curve to confirm specificity. MtDNA copy number was calculated as 2 × (2^ΔCt), with ΔCt = nCt - mtCt, which is inversely proportional to mtDNA content[16].

Human osteoclast differentiation.

Human peripheral blood mononuclear cells (PBMCs) were isolated from EDTA-blood of healthy donors and MELAS patients. The PBMCs were centrifuged and resuspended in 10% DMSO in FBS and stored in -80° C. On the day of seeding (day -3), 2.5×10^5 cells/well of human PBMCs were seeded in 96-well plates with 100 µL/well of Alpha-MEM culture media containing 100 ng/ml human M-CSF, 10% FBS, 1% pen/strep, and 1% L-glutamine. This setup was maintained at 37°C in a 5.5% CO2 humidified incubator for 72 hours to facilitate the purification of adherent cells through plastic adhesion. On day 0, the cells were induced to differentiate into OCs in 100 µL/well of complete osteoclastogenic media (Alpha-MEM culture media with 10% FBS, 1% pen/strep, and 1% L-glutamine) supplemented with 50 ng/ml human M-CSF and 100 ng/ml human RANKL, and spermidine at 10uM. Subsequently, the culture medium was refreshed on day 2 and day 4. By day 6, mature OCs had formed and were fixed using 4% PFA for TRAP analysis.

Phenotypes and m.3243A>G in UK Biobank

The UK Biobank (UKB) is a population cohort of approximately 500,000 individuals from the UK[17]. As of 2024, it provides whole genome sequencing data alongside comprehensive phenotypic information, including electronic health records from hospitals and general practitioners, as well as self-reported data, death records, and cancer registry data. Heel bone mineral density (BMD) measurements using the Sahara heel ultrasound device are available for 278,835 participants, while DXA imaging-derived BMD data exist for 47,757 participants. Our study utilized the subset of UK Biobank participants with either ultrasound or DXA-derived BMD measurements. Our primary bone phenotype incorporated clinically relevant features, including self-reported fracture (data field 2463) as a surrogate for fragility fracture, consistent with previous publications[18]. We also analyzed direct BMD measurements from heel, spine (L1-L4), femur neck, and total body scans, using the minimum value between left and right measurements where available. The characteristics of the included cohort are detailed in Supplementary Table 2.

Mitochondrial m.3243A>G analysis. We identified the mitochondrial DNA (mtDNA) m.3243A>G variant using mitoHPC on UKB DRAGEN CRAM files[19]. The detailed process of variant and sample filtering is described in our recent publication. We successfully processed 490,412 samples to identify the m.3243A>G variant, a known pathogenic variant associated with diabetes and deafness[19]. For this study, we restricted our analysis to individuals with either heel or DXA imaging data. The characteristics of the included cohort are provided in Supplementary Table 2-4. We employed linear regression models to test the association between m.3243A>G and bone phenotypes, adjusting for age, age squared, sex, weight, principal components, assessment center, and sequencing center. A sensitivity analysis was performed, limiting the sample to individuals with >10%

heteroplasmy. We used Fisher's exact test to analyze the association between self-reported fracture and diabetes with m.3243A>G carrier status, using diabetes as a positive control for this analysis. We used Bonferroni corrected p value (0.05/4 = 0.0125) for linear regressions for significance threshold.

Statistical analysis

The mean±standard error of the mean (SEM) was used to represent all data. When comparing two experimental groups, a two-tailed t-test was employed. For datasets that were normally distributed with equal variances, an unpaired two-tailed Student's t-test was utilized. In experiments that had ≥3 experimental groups, one-way analysis of variance (ANOVA) and multiple comparisons with Tukey's correction were employed. Paired or unpaired one-way ANOVA was utilized for multiple comparisons of normally distributed datasets with one variable. The p-value was applied to evaluate the statistical significance of the hypothesis being tested. GraphPad Prism (San Diego, CA, Version 9.5.1 (528)) was used for statistical analyses. Wilcoxon rank-sum tests were used in single-cell statistical testing in R (v4.2.2).

3D bone reconstruction

To reconstruct and visualize the bone, Algorithm 1 is used (Supplementary Table 1). First, the CT volumes are rotated and translated to a standard position and orientation. Next, binary volumes of the entire skeleton structure and the cortical bones are extracted from the input volumes through thresholding. Subsequently, the connected components in the binary volumes are counted. This step aids in removing the fibular bone and retaining the largest connected cortical bone, as facilitated by Algorithm 2. Thereafter, the largest cortical bone is dilated and then eroded to fill the hole inside the tibia using Algorithm 3. In the final step, the cortical bones with filled holes intersect with the tibial skeleton structure, excluding the fibula, to extract the 3D shape of the tibial bone in the region of interest.

In Algorithm 2, a binary volume V^i and the index k serve as inputs (Supplementary Table 1). The initial step involves identifying and counting the connected components using MATLAB's built-in function "bwconncomp()". In the subsequent step, the connected components within the binary volume are labeled and tallied using MATLAB's built-in functions "labelmatrix()" and "regionprops()". These connected components are then arranged in descending order using MATLAB's "sort()" function. The value of index k is assessed to determine whether it's positive or negative. If k is positive, the kth largest component is retained while others are discarded; if k is negative, the kth largest component is eliminated. The algorithm concludes by outputting the remaining components, V^o. As a result, this methodology is adept at removing the fibular bone and any extraneous fragments that lie outside the tibial bone.

Algorithm 3 takes a binary volume V^i and a series of iteration numbers for dilation or erosion $[t_1, t_2, \cdots t_k]$ as inputs (Supplementary Table 1). The structuring element is initialized using MATLAB's built-in function "strel()". Subsequently, for each iteration number designated for dilation or erosion, the iteration number t is examined. If t is positive, the copied binary volume V^o undergoes t dilation iterations, and if t is negative, V^o is eroded for t times. This algorithm is thus integrated into Algorithm 1 with the aim of filling holes inside the cortical bones and subsequently compressing the volume to adhere to the original bone size.

Quantification of OC and OB from in vitro staining

To quantify the OC and OB parameters from microscopic images, Algorithm 4 is employed to determine the area size and the ratio of the cell region. In Algorithm 4, each image is processed using its corresponding mask for the region of interest and specific thresholding values (Supplementary Table 1). The algorithm starts by normalizing the intensity of the input images. Subsequently, the red channel of the image is extracted through thresholding to identify and isolate the cell areas. The next step involves identifying and counting the connected components with MATLAB's built-in function "bwconncomp()". Following that, the connected components within the binary image are labeled and enumerated using MATLAB's "labelmatrix()" and "regionprops()" functions. For each connected component, excluding the background region, the area size and its ratio in the entire region of interest

are computed based on the areas of the red channels. As a result, this algorithm can accentuate the cell regions in the provided images and compute the OC and OB parameters from the given microscopic imagery.

1. Lechuga-Vieco, A. V. *et al.* Heteroplasmy of Wild-Type Mitochondrial DNA Variants in Mice Causes Metabolic Heart Disease With Pulmonary Hypertension and Frailty. *Circulation* **145**, 1084–1101 (2022).
2. Leng, H. *et al.* Modulating glycosphingolipid metabolism and autophagy improves outcomes in pre-clinical models of myeloma bone disease. *Nat Commun* **13**, 7868 (2022).
3. Bakewell, S. J. *et al.* Platelet and osteoclast β_3 integrins are critical for bone metastasis. *Proc. Natl. Acad. Sci. U.S.A.* **100**, 14205–14210 (2003).
4. Alsaleh, G. *et al.* Autophagy in T cells from aged donors is maintained by spermidine and correlates with function and vaccine responses. *eLife* **9**, e57950 (2020).
5. Korsunsky, I. *et al.* Fast, sensitive and accurate integration of single-cell data with Harmony. *Nat Methods* **16**, 1289–1296 (2019).
6. Fang, H., Knezevic, B., Burnham, K. L. & Knight, J. C. XGR software for enhanced interpretation of genomic summary data, illustrated by application to immunological traits. *Genome Med* **8**, 129 (2016).
7. Bergen, V., Lange, M., Peidli, S., Wolf, F. A. & Theis, F. J. Generalizing RNA velocity to transient cell states through dynamical modeling. *Nat Biotechnol* **38**, 1408–1414 (2020).
8. Lange, M. *et al.* CellRank for directed single-cell fate mapping. *Nat Methods* **19**, 159–170 (2022).
9. Wolf, F. A. *et al.* PAGA: graph abstraction reconciles clustering with trajectory inference through a topology preserving map of single cells. *Genome Biol* **20**, 59 (2019).
10. Dann, E., Henderson, N. C., Teichmann, S. A., Morgan, M. D. & Marioni, J. C. Differential abundance testing on single-cell data using k-nearest neighbor graphs. *Nat Biotechnol* **40**, 245–253 (2022).
11. Lareau, C. A. *et al.* Massively parallel single-cell mitochondrial DNA genotyping and chromatin profiling. *Nat Biotechnol* **39**, 451–461 (2021).
12. Curtabbi, A. *et al.* Regulation of respiratory complex I assembly by FMN cofactor targeting. *Redox Biology* **69**, 103001 (2024).
13. Acín-Pérez, R., Hernansanz-Agustín, P. & Enríquez, J. A. Analyzing electron transport chain supercomplexes. in *Methods in Cell Biology* vol. 155 181–197 (Elsevier, 2020).

14. Schindelin, J. *et al.* Fiji: an open-source platform for biological-image analysis. *Nat Methods* **9**, 676–682 (2012).

15. Lechuga-Vieco, A. V. *et al.* Cell identity and nucleo-mitochondrial genetic context modulate OXPHOS performance and determine somatic heteroplasmy dynamics. *Sci. Adv.* **6**, eaba5345 (2020).

16. Moreno-Loshuertos, R. *et al.* Differences in reactive oxygen species production explain the phenotypes associated with common mouse mitochondrial DNA variants. *Nat Genet* **38**, 1261–1268 (2006).

17. Bycroft, C. *et al.* The UK Biobank resource with deep phenotyping and genomic data. *Nature* **562**, 203–209 (2018).

18. Kemp, J. P. *et al.* Identification of 153 new loci associated with heel bone mineral density and functional involvement of GPC6 in osteoporosis. *Nat Genet* **49**, 1468–1475 (2017).

19. Cannon, S. J. *et al.* Penetrance and expressivity of mitochondrial variants in a large clinically unselected population. *Human Molecular Genetics* **33**, 465–474 (2024).

Figure Legends

Figure 1. Heteroplasmic mice exhibit increased bone density and mechanical strength due to osteoclast dysfunction.

A Representative micro-CT reconstructed images of tibiae from 12-14-week-old male BL/6^{C57}, BL/6^{NZB} and BL/6$^{C57\text{-}NZB}$ mice.

B–**C** Micro-CT analysis of bone morphology parameters: BV/TV (bone volume fraction), Tb.Th (trabecular thickness), BS/BV (bone surface density), Tb.Sp (trabecular separation), Ct.Th (cortical thickness) and Ct.Ar (BL/6^{C57}, $n = 9$; BL/6^{NZB}, $n = 12$; and BL/6$^{C57\text{-}NZB}$, $n = 10$; each dot represents tibial measurements from an individual animal).

D Schematic overview illustrating the positioning of femur for compression testing between the load area and the platform load frame (left). Representative load displacement curve of femur from the BL/6^{C57} control group (middle). Dot plot showing the maximum load values for the femur in 12- to 14-week-old males of the indicated genotypes (right). BL/6^{C57}, $n = 8$; BL/6^{NZB}, $n = 8$; and BL/6$^{C57\text{-}NZB}$, $n = 7$. Each dot represents femoral measurements from an individual animal).

E Representative TRAP/0.2% methyl green-stained tibial sections showing osteoclasts (red/purple, black arrowheads) on the endocortical bone surface in BL/6^{C57}, BL/6^{NZB} and BL/6$^{C57\text{-}NZB}$ mice (n=5, two independent experiments).

F Bone histomorphometric quantification of osteoclasts (OCs), including the percentage of OC surface relative to the total bone surface (Oc.S/BS; left) and average length (right) (BL/6^{C57}, $n = 10$; BL/6^{NZB}, $n = 9$; and BL/6$^{C57\text{-}NZB}$, $n = 10$ mice, each dot represents an individual animal).

G ELISA analysis of serum levels of CTX-1 (left) and PINP (right) (n = 16 mice from the indicated genotypes, with each dot representing one animal.).

In A-G: *$p < 0.05$, **$p < 0.01$; ***$p < 0.001$, ****$p < 0.0001$ determined by ANOVA test. Data are presented as mean ± SEM.

H-I Lethally irradiated 8-week-old CD45.1+ B6.SJL and BL/6$^{C57\text{-}NZB}$ CD45.1+ mice were reconstituted with BM cells from female BL/6^{C57} CD45.2+ or BL/6$^{C57\text{-}NZB}$ CD45.2+ mice. After 9 weeks, micro-CT analysis was performed on tibiae. Left: Representative micro-CT reconstructed images. Right: BV/TV quantification (BL/6^{C57} to CD45.1+ B6.SJL, n = 10; BL/6$^{C57\text{-}NZB}$ to CD45.1^{+} B6.SJL, n = 12; BL/6^{C57} to BL/6$^{C57\text{-}NZB}$, n = 10; BL/6$^{C57\text{-}NZB}$ to BL/6$^{C57\text{-}NZB}$, n = 8; each dot represents an individual animal). *$p < 0.05$, two-way ANOVA.

Supplementary Figure 1: Gating strategy and quantification for OC progenitors and bone marrow chimera reconstitution.

A Flow cytometry gating strategy of the OC progenitors (CD11b- B220- CD3- CD115+) in BM cells (left) and percentage of OC progenitors (right) from BL/6^{C57} mice (n=10), BL/6^{NZB} mice (n=8) and BL/6$^{C57\text{-}NZB}$ (n=9) mice.

B Assessment of reconstitution efficacy in chimeric mice by evaluating the BM CD45.2+ population. Each dot represents an individual animal. Filled dots: donor cells; Empty dots: endogenous cells.

C Representative flow cytometry plots showing the gating strategy and distribution of CD45.1+/CD45.2+ BM cells from the specified groups.

D Morphological bone parameters in tibiae measured by micro-CT. Tb.Th, BS/BV, Tb.Sp, Ct.Th and Ct.Ar (BL/6^{C57} to CD45.1+ B6.SJL group (n=10); BL/6$^{C57\text{-}NZB}$ to CD45.1^{+} B6.SJL group (n=12); BL/6^{C57} to BL/6$^{C57\text{-}NZB}$ group (n=10); BL/6$^{C57\text{-}NZB}$ to BL/6$^{C57\text{-}NZB}$ group (n=8).

In A-D: each dot represents and individual animal. *$p < 0.05$, **$p < 0.01$; ***$p < 0.001$, ****$p < 0.0001$ determined by two-way ANOVA test. Data are presented as mean ± SEM.

Figure 2. Impaired osteoclast differentiation, with mitochondrial dysfunction emerging as a hallmark in the first 3 days.

A Bone marrow cells from 8-week-old mice BL/6^{C57} , BL/6^{NZB} and BL/6$^{C57\text{-}NZB}$ mice were differentiated into osteoclasts (OCs) using 10 ng/ml M-CSF and 50 ng/ml RANKL. OCs were identified by TRAP staining on day 5 (left) Scale bar: 200 µm. The percentage of OC area relative to the total area was quantified (right). N= 20 mice per genotype (four independent experiments; each dot represents and individual animal). ****$p < 0.0001$ determined by one-way ANOVA test. Data are presented as mean ± SEM.

B Schematic of experimental strategy for single-cell transcriptomics of murine osteoclast formation. Bone marrow cells from BL/6^{C57} (n=3), BL/6^{NZB} (n=3), and BL/6$^{C57\text{-}NZB}$ (n=3) strains were isolated and cultured with M-CSF (10 ng/ml) for 2 days, followed by M-CSF (10 ng/ml) and RANKL (50 ng/ml) from day 0 to day 3. Single-cell sequencing and analysis were then performed with day 0, day 1 and day 3 cells.

C Expression levels of osteoclast marker genes (*Acp5* and *Ctsk*) from aggregated single cells at each time point, indicating successful *in vitro* osteoclastogenesis.

D Uniform manifold approximation and projection (UMAP) visualization of single-cell transcriptomic profiles (n = 10,809 cells) during osteoclast differentiation. Cells are clustered by transcriptomic similarity and shown at three time points: day 0, day 1, and day 3.

E UMAP visualization of 10,809 cells during osteoclast differentiation, clustered by transcriptomic similarity and shown at day 0, day 1, and day 3 for different mtDNA groups (BL/6^{C57}, BL/6^{NZB}, and BL/6C$^{57\text{-}NZB}$).

F GO-BP pathway enrichment analysis for genes upregulated (red) or downregulated (blue) in BL/6$^{C57\text{-}NZB}$ osteoclasts compared to BL/6^{C57} osteoclasts.

Supplementary Figure 2. Single-cell transcriptomic profiling and trajectory analysis of *in vitro* osteoclast formation.

A UMAP visualization of the expression levels of osteoclasts marker genes (*Acp5*, *Mmp9, Ctsk, Dcstamp,* and *Ocstamp*) and negative regulators (*Irf8*, *Bcl6*, and *Mafb*). Color indicates log-normalized gene expression levels.

B UMAP projection of velocity-latent time estimated from the RNA splicing dynamics. Cells with a latent time of 0 or 1 represent the starting or terminating population infered by RNA velocity, respectively.

C A fate map for osteoclast differentiation using directed probabilistic approximate graph abstraction (PAGA). Each node represents one cluster in Figure 2D and arrows represent aggregated velocity flow concordant to the velocity-inferred trajectory. Dotted lines represent other velocity flow between each pair of clusters. Pie charts denote the relative abundance of BL/6^{C57}, BL/6^{NZB} and BL/6$^{C57\text{-}NZB}$ cells, normalized by the total number of cells in each group. The relative abundance of BL/6$^{C57\text{-}NZB}$ cells for each cluster along the osteoclast differentiation trajectory is labelled next to the pie chart.

D A graph representation of differential abundance tests. The relative enrichment BL/6$^{C57\text{-}NZB}$ cells in early-stage pre-osteoclasts (shown in red), as well as the relative depletion in mature osteoclasts (shown in blue), indicates premature termination of osteoclastogenesis in heteroplasmic cells. Nodes represent neighbourhoods of cells with similar transcriptomic profiles, colored by the relative abundance ($\log_2$FC) of BL/6$^{C57\text{-}NZB}$ cells compared to BL/6^{C57}. Node sizes correspond to the number of cells in a neighbourhood. Non-significant neighbourhoods ($p>0.05$) are colored in white and plotted in the background.

Figure 3. Osteoclast maturation requires OXPHOS function which is disrupted by heteroplasmy, due to impaired localisation of complex I

A Heatmap showing gene expression changes for genes encoding subunits of respiratory ketogenesis, the Krebs cycle, pyrimidine biosynthesis and Complex I in osteoclasts derived from BL/6$^{C57\text{-}NZB}$ compared to BL/6^{C57} mice at day 0, day 1, and day 3 (n=3 mice per genotype).

B Aggregated expression of OXPHOS genes (OXPHOS scores) of *in vitro* OCs from different clusters (1-8) derived from BL/6^{C57}, BL/6^{NZB}, and BL/$^{6C57\text{-}NZB}$ mice (n=3 animals per genotype). Module expression scores were normalized by subtracting the aggregated expression levels of a randomly selected, expression matched control gene set.

C Oxygen consumption rate (OCR) of intact cells estimated by SeaHorse during OC differentiation at day 0, day 1, and day 3 (3 to 5 independent assays per biological sample)

D Ratio of Complex I to Complex II activities. Respiratory complexes activities were measured spectrophotometrically using 5 µg of total mitochondrial protein per assay. Measurements were performed in four replicates using pre-OCs on days 0 and 3 of differentiation.

E Total ATP levels assessed by luminometry on day 1 and day 3 of osteoclast differentiation from BL/6^{C57}, BL/6^{NZB}, and BL/6$^{C57\text{-}NZB}$ mice. Each dot represents *in vitro* osteoclast differentiation from an individual mouse of the indicated genotypes. ** $p < 0.01$, determined using Tukey's multiple comparisons following two-way ANOVA.

F-G Confocal imaging of mitochondrial TOM20, Complex I subunit NDUFA9 and Complex V subunit ATPB in pre-osteoclasts on day 3 of differentiation derived from BL/6^{C57}, BL/6^{NZB}, and BL/6$^{C57\text{-}NZB}$ mice. F: Protein expression quantification ratio of NDUFA9 and ATPB per mitochondrion (NDUFA9/TOM20; ATPβ/TOM20), based on marker signals (Integrated Density, IntDen) on day 3 (n=4 mice per genotype). G: Representative confocal images for the indicated markers. Scale bar: 5 µm, n = 4 mice per genotype. * $p < 0.05$, two-tailed Dunnett's test following one-way ANOVA.

In C-F data are presented as mean values ± SEM.

Supplementary Figure 3. Transcriptomic analysis of metabolic pathways and mitochondrial characterization during osteoclast differentiation

A Heatmap showing gene expression changes for genes involved in glycolysis, glutamate degradation, adenosine biosynthesis, and the pentose phosphate pathway in osteoclasts cultures derived from BL/6$^{C57\text{-}NZB}$ and BL/6^{C57} mice at day 0, day 1, and day 3 (n=3 mice per genotype).

B Spare respiratory capacity (SRC) calculated by subtracting basal respiration from maximal respiration during *in vitro* osteoclast differentiation (day 0 to day 3) for the indicated genotypes. Data are presented as mean ± SEM (n=5, two independent experiments). *$p < 0.05$, two-tailed Dunnett's test following one-way ANOVA..

C Mitochondrial content was assessed using N-acridine orange (NAO) staining. Live cells were analyzed by FACS during osteoclast differentiation from day 0 to day 3.

D ROS quantification on day 0, day 1 and day 3 during OC differentiation. Left: Quantification of CellROX Deep Red MFI measurements (left) . Each dot represents an individual mouse. Right: FACS histogram plot (left) are representative measurements from untreated (grey), cells derived from BL/6^{C57} (blue), BL/6^{NZB} (red) BL/6$^{C57\text{-}NZB}$ (green) mice, where the grey line show background MFI (unstained).

In C-D, data were normalized to wild-type BL/6^{C57}; n= 3 BL/6^{C57} n=3 BL/6^{NZB} and n=5 BL/6$^{C57\text{-}NZB}$. * p<0.05, ** p <0.01 determined using Tukey's multiple comparisons following two-way ANOVA.

E Western blot analysis for OXPHOS complexes protein expression in day 0 , day 1 and day 3 of *in vitro* OC differentiation. CI-NDUFB8, CII-SDHB, CIII-UQCRC2, CIV-MTCO1 and CV-ATP5A levels are shown. TOM20 expression was used as mitochondrial protein loading control. Representative image from four independent experiments, n=4 mice per genotype.

In B-G, data are presented as mean values ± SEM.

Figure 4. Impaired import of nuclear-encoded complex I subunits into mitochondria leads to disrupted supercomplex assembly in heteroplasmic cells.

A-B: Confocal imaging of mitochondrial TOM20, Complex I subunit NDUFA9 and DAPI in pre-osteoclasts on day 3 of differentiation (A) and mature osteoclasts on day 5 of differentiation (B) derived from BL/6^{C57}, BL/6^{NZB}, and BL/6$^{C57\text{-}NZB}$ mice. Left: Representative confocal images for the indicated markers. Right: Quantification of colocalization of Complex I in the mitochondria (TOM20/NDUFA9) using as a control colocalization between mitochondria and the nucleous (TOM20/DAPI), shown by Pearson's coefficient. Scale bar: 5 µm, n = 4 mice per genotype. * p <0.05, *** p < 0.001, **** p < 0.00001, two-tailed Dunnett's test following one-way ANOVA. In A-B, data are presented as mean values ± SEM.

C-E Heatmap showing gene expression changes for genes involved in the mitochondrial protein import machinery (C), mitochondrial degradome (D) and mitochondrial assembly factors (E) in osteoclasts cultures derived from BL/6$^{C57\text{-}NZB}$ and BL/6^{C57} mice at day 0, day 1, and day 3 (n=3 mice per genotype).

In A-C, data are presented as mean values ± SEM.

Supplementary Figure 4. Mitochondrial-encoded genes are upregulated at day 3 of OC differentiation

A Violin plots displaying the average expression levels of mitochondrial DNA-encoded genes in BL/6^{C57} cells at day 0 (n = 1,550), day 1 (n = 1,148), and day 3 (n = 1,292) during OC differentiation. Complex I: mt-Nd1, mt-Nd2, mt-Nd3, mt-Nd4, mt-ND4L, mt-Nd5 and mt-Nd6. Complex III: mt-Cytb. Complex IV: mt-Co1, mt-Co2 and mt-Co3. Complex V (ATPase): mt-Atp6 and mt-Atp8. The y-axis represents the depth-normalized gene expression level in log scale (log count per 10,000 sequencing reads). **** p < 0.0001, Wilcoxon test, with day 0 and day 1 cells as the reference groups.

B Confocal imaging of mitochondrial TOM20 (red), Complex I subunit NDUFA9 (cyan) and DAPI (grey) in pre-osteoclasts on day 1 of differentiation derived from BL/6^{C57}, BL/6^{NZB}, and BL/6$^{C57\text{-}NZB}$ mice. Representative confocal images for the indicated markers. Scale bar: 5 µm, n = 4 mice per genotype. blurry

Figure 5. Mitochondrial selection during vitro OC maturation, and exhausted autophagic flux can be restored in heteroplasmic cells with spermidine

A NZB mtDNA levels (estimated as a percentage of total mtDNA) from BL/6$^{C57\text{-}NZB}$ mice, showing a shift toward mtDNA^{NZB} haplotype in day 3 cells compared to day 1. Each dot represents one cell and is colored by the percentile-normalized sequencing coverage of mtDNA^{NZB} variants. The colour scale represents sequencing depth. day 1: n = 1,249 cells; day 3: n = 884 cells. Median values are marked by black lines. **** $p < 0.0001$, Wilcoxon test.

B Assessment of the heteroplasmy shift toward NZB mtDNA at day 3 compared to day 1 in pre-OCs derived from BL/6$^{C57\text{-}NZB}$ young mice (n=9; each dot represents an individual mouse). The transformed heteroplasmy shift was evaluated using day 0 as the reference for each heteroplasmic mouse. NZB mtDNA levels were quantified by PCR, followed by RFLP (Restriction Fragments Length Polymorphism) to distinguish between C57 and NZB mtDNA variants. * $p < 0.05$, unpaired t test.

C NZB mtDNA levels in BL/6$^{C57\text{-}NZB}$ cells across different clusters indicating increased mitochondrial segregation in osteoclasts compared to monocytic precursors. Median values are marked by grey lines. **** $p < 0.0001$, Wilcoxon test, with monocytic precursors as the reference group.

D-E Western Blot analysis of autophagy in primary murine BM cells treated with M-CSF and RANKL for 1 or 3 days. (D) Representative images of membranes showing p62 and LC-3 expression and (E) autophagy flux quantification of the LC-3 bands (LC3-I/LC3-II) at day 1 and 3 of OC differentiation. 10 nM BafA1 was added 2 hours before protein harvest, with actin used as a loading control. n = 8 independent biological samples for DMSO control and BafA. **$p < 0.01$, ****$p < 0.0001$, two-way ANOVA with Sidak's multiple comparisons test.

Quantification of autophagy flux based on LC3-I/LC3-II band intensity from western blot analysis after day 1 of OC differentiation. BafA1 (10 nM) was added 2 hours before protein harvest. n = 8 independent biological samples for both DMSO control and BafA1 treatment.).

F-G Bone marrow cells from 8-week-old mice BL/6^{C57}, BL/6^{NZB} and BL/6$^{C57\text{-}NZB}$ mice were differentiated into osteoclasts (OCs) using 10 ng/ml M-CSF and 50 ng/ml RANKL with or without 10 uM spermidine (spd) treatment. F: The percentage of OC area relative to the total area was quantified. Data are representative of two independent

experiments. * $p < 0.05$, ****$p < 0.0001$, nonparametric Kruskal-Wallis test. G: OCs were identified by TRAP staining on day 5. Scale bar: 50 µm.

H Assessment of the heteroplasmy shift toward NZB mtDNA at day 5 in OCs derived from BL/6^{C57-}NZB young mice (n=10 for untreated and n=8 for cultures treated with 10 µM spermidine; each dot represents an individual mouse). The transformed heteroplasmy shift was evaluated using day 1 as the reference for each heteroplasmic mouse. NZB mtDNA levels were quantified by PCR, followed by RFLP (Restriction Fragments Length Polymorphism) to distinguish between C57 and NZB mtDNA variants. ** $p < 0.01$, nonparametric Mann-Whitney test.

I Total ATP levels were measured by luminometry on day 3 of OC differentiation in BL/6^{C57}, BL/6^{NZB}, and BL/6$^{C57-NZB}$ mice, with and without 10 µM spermidine treatment. Data are normalized to untreated cells and each dot represents a sample from an individual mouse of the indicated genotype. ****$p < 0.0001$, one-way ANOVA and Sidak's multiple comparison test.

J Confocal imaging of mitochondrial TOM20, Complex I subunit NDUFA9, and ATPase subunit ATPB in pre-osteoclasts derived from BL/6^{C57}and BL/6^{NZB}, and BL/6$^{C57-NZB}$ mice with and without spermidine treatment on day 5 of *in vitro* OC differentiation. Left: Protein quantification ratio of NDUFA9 per mitochondrion (NDUFA9/TOM20), based on marker signals (Integrated Density, IntDen)(n=3 mice per genotype). **** $p <0.0001$, two-tailed Dunnett's test following one-way ANOVA. Right: Representative confocal images for the indicated markers in pre-osteoclasts derived from BL/6$^{C57-NZB}$ mice with and without spermidine treatment on day 5 of *in vitro* OC differentiation. Scale bar: 5 µm.

K-L Lethally irradiated young BL/6$^{C57-NZB}$ mice were reconstituted with bone marrow from BL/6^{C57} or BL/6$^{C57-NZB}$ mice and treated with 5 mM spermidine in drinking water for 8 weeks. (K) Representative micro-CT reconstructed images of tibiae from the bone marrow reconstituted mice. (L) BV/TV, Tb.Th, BS/BV Tb.Sp, Ct.Th and Ct.Ar of tibiae quantification by micro-CT (n = 8 BL/6^{C57}; n = 6 BL/6$^{C57-NZB}$ and n = 7 BL/6$^{C57-NZB}$+Spd; each dot represents an individual animal). The experiment is representative of two independent experiments. *$p < 0.05$, **$p < 0.01$, ***$p < 0.001$, ****$p < 0.0001$, one-way ANOVA followed by Tukey's multiple comparisons test.

M Bending test analysis in bone marrow transplanted mice treated with 5 mM spermidine. Dot plots of maximum femur load from bone marrow-transplanted mice, assessed using the bending test (n = 5 mice per BM cell genotype; each dot represents an independent animal). *$p < 0.05$, **$p < 0.01$, one-way ANOVA followed by Tukey's multiple comparisons test.

In B-M, data are presented as mean values ± SEM.

Supplementary Figure 5. Analysis of Mitochondrial Selection and the Role of Autophagy and Spermidine Supplementation in In Vitro and In Vivo Osteoclastogenesis

A Average sequencing depth (bars) and the average heteroplasmic percentage (dots) for selected NZB mtDNA variants in heteroplasmic cells. Colors represent the number of cells with at least 10x coverage for a given variant.

B NZB mtDNA levels (%NZB mtDNA, y axis) plotted against the velocity latent time (x axis, same latent time as shown in Supplementary Figure 2B), demonstrating a slight shift towards NZB mtDNA during osteoclast differentiation. *** $p < 0.001$, Spearman's rank correlation test.

C Assessment of the percentage of NZB mtDNA (% NZB mtDNA) during *in vitro* OC differentiation of heteroplasmic cells (0, 48, and 192 hours after the addition of 10 ng/ml M-CSF and 50 ng/ml RANKL). NZB mtDNA levels were quantified by PCR, followed by RFLP (Restriction Fragment Length Polymorphism) to distinguish between C57 and NZB mtDNA variants. Samples were derived from n = 4 BL/6$^{C57\text{-}NZB}$ mice.

D Quantification of p62 expression from Western blot analyses shown in Figure 5D. 10 nM BafA1 was added 2 hours before protein harvest, with actin used as a loading control. n = 8 independent biological samples for DMSO control and BafA1; each dot represents an individual mouse. *$p < 0.05$, **$p < 0.01$, determined using Tukey's multiple comparisons following two-way ANOVA.

E Violin plots displaying the average expression levels of Tfeb in monocytic precursors (Mono) and mature osteoclasts (OC) in BL/6^{C57} (black), BL/6^{NZB} (grey), and BL/6$^{C57\text{-}NZB}$ mice (red).*$p < 0.05$, ***$p < 0.001$, two-sided Wilcoxon test.

F Mitochondrial DNA copy numbers in BL/6$^{C57\text{-}NZB}$ cell cultures with or without 5 μM spermidine treatment on day 1 and day 3 during osteoclast differentiation (n=4-5 mice). mtDNA copy numbers were normalized to genomic DNA copy numbers, as determined by qPCR ($2^{-\Delta CT}$).

G Total ATP levels were measured by luminometry on day 1 of OC differentiation in BL/6^{C57}, BL/6^{NZB}, and BL/6$^{C57\text{-}NZB}$ mice, with and without 10 μM spermidine treatment. Data are normalized to untreated cells and each dot represents a sample from an individual mouse of the indicated genotype. ****$p < 0.0001$, one-way ANOVA and Sidak's multiple comparison test.

H-I Confocal imaging of mitochondrial TOM20, Complex I subunit NDUFA9, and ATPase subunit ATPB in pre-osteoclasts derived from BL/6^{C57}and BL/6^{NZB}, and BL/6$^{C57\text{-}NZB}$ mice with and without spermidine treatment on day 5 of *in vitro* OC differentiation. I: Protein quantification ratio of ATPB per mitochondrion (ATPB/TOM20), based on marker signals (Integrated Density, IntDen)(n=3 mice per genotype). **** $p <0.0001$, *** $p <0.001$, ** $p <0.01$, two-tailed Dunnett's test following one-way ANOVA. In A-B, data are presented as mean values ± SEM. J:

Representative confocal images for the indicated markers in pre-osteoclasts derived from BL/6^{C57}and BL/6^{NZB} mice with and without spermidine treatment on day 5 of *in vitro* OC differentiation. Scale bar: 5 µm.

Figure 6. Osteoclast differentiaion in cells from patients with mtDNA heterogeneity (m.3243A>G) is impaired and can be restored with spermidine

A Human PBMCs were seeded and differentiated into osteoclasts (OCs) using 50 ng/ml human M-CSF and 75 ng/ml human RANKL. Left: Representative images of TRAP staining from OC on day 9. Right: Quantification of the percentage of OC area relative to the total area. n=3 healthy donors (HD) and n=5 m.3243A>G patients; 3 technical replicates per condition. * $p < 0.05$, two-tailed unpaired t-test.

B Quantification of bone resorption marker CTX-1 levels in human serum samples from healthy donors (HD, n=10) and m.3243A>G patients (n=5). *$p < 0.05$, two-tailed unpaired t-test.

C Human PBMCs were seeded and differentiated into osteoclasts (OCs) in the presence of 50 ng/ml human M-CSF and 75 ng/ml human RANKL, with or without 10 µM spermidine treatment. Left: Representative images of TRAP staining from OC on day 6. Right: Quantification of the percentage of OC area relative to the total area. n=4 healthy donors (HD) and n=4 m.3243A>G patients; 6 technical replicates per condition. ** $p < 0.01$, determined using Tukey's multiple comparisons following one-way ANOVA. Scale bar: 50 µm.

D Total ATP levels assessed by luminometry on day 5 of osteoclast differentiation from human PBMCs in the presence of 50 ng/ml human M-CSF and 75 ng/ml human RANKL, with or without 10 µM spermidine treatment. Each dot represents *in vitro* osteoclast differentiation from a donor. n=5 healthy donors (HD) and n=5 m.3243A>G patients. * $p < 0.05$, determined using Tukey's multiple comparisons following one-way ANOVA.

In A-D, data are presented as mean values ± SEM.

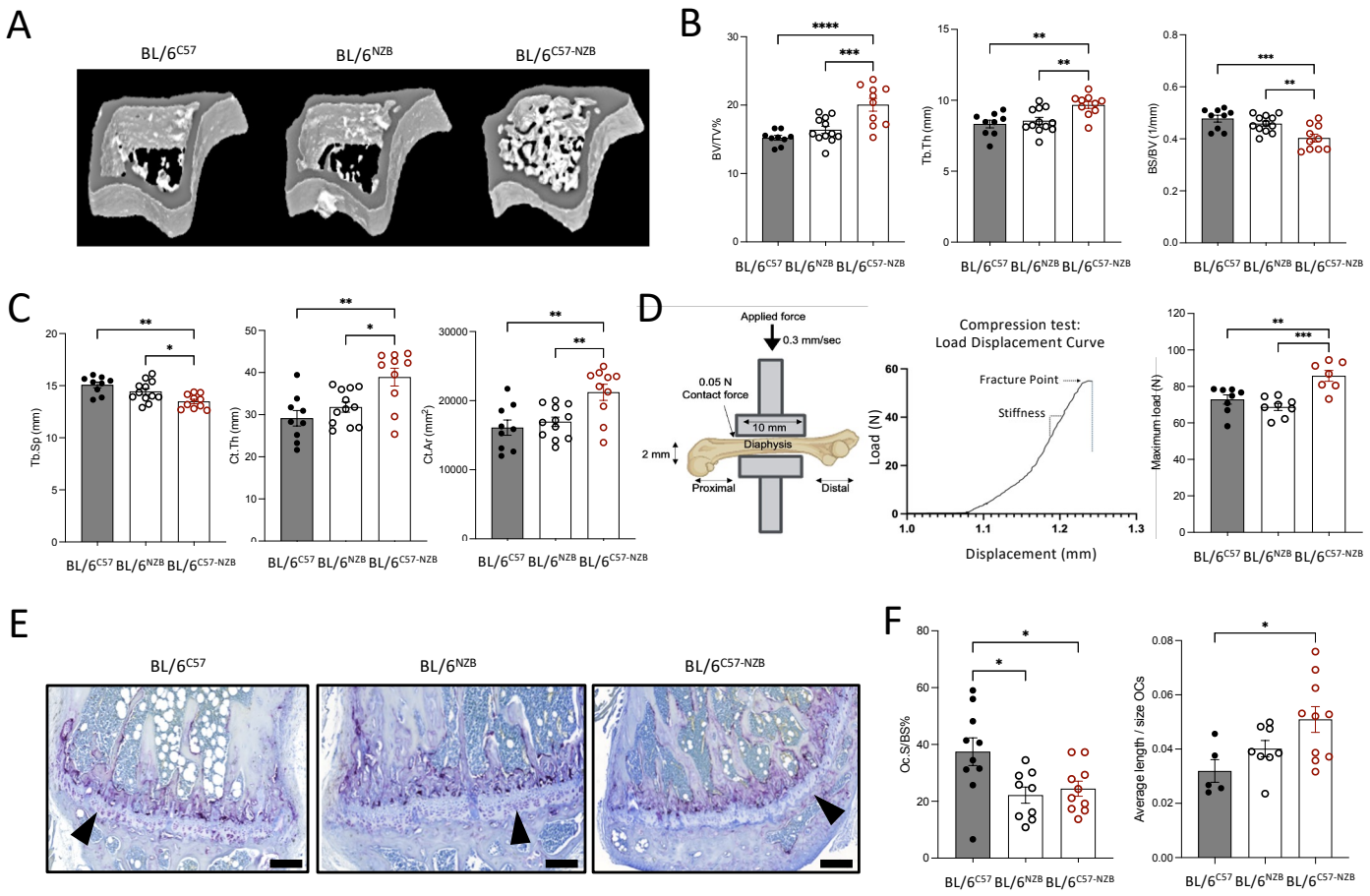
A
BL/6C57
BL/6NZB
BL/6C57-NZB
B
BV/TV%
Tb.Th (mm)
BS/BV (1/mm)
C
Tb.Sp (mm)
Ct.Th (mm)
Ct.Ar (mm²)
D
Applied force
0.3 mm/sec
0.05 N
Contact force
10 mm
Diaphysis
2 mm
Proximal
Distal
Compression test:
Load Displacement Curve
Fracture Point
Stiffness
Load (N)
Displacement (mm)
Maximum load (N)
E
F
Oc.S/BS%
Average length / size OCs
G
Serum CTX1 (ng/ml)
Serum PINP (ng/ml)
H
Host:BL/6C57
Host: BL/6C57-NZB
BM:
C57 mtDNA
BM:
C57-NZB mtDNA
I
Donor
BM: C57-NZB mtDNA
BM: C57 mtDNA
BV/TV%
Host:

Figure 1

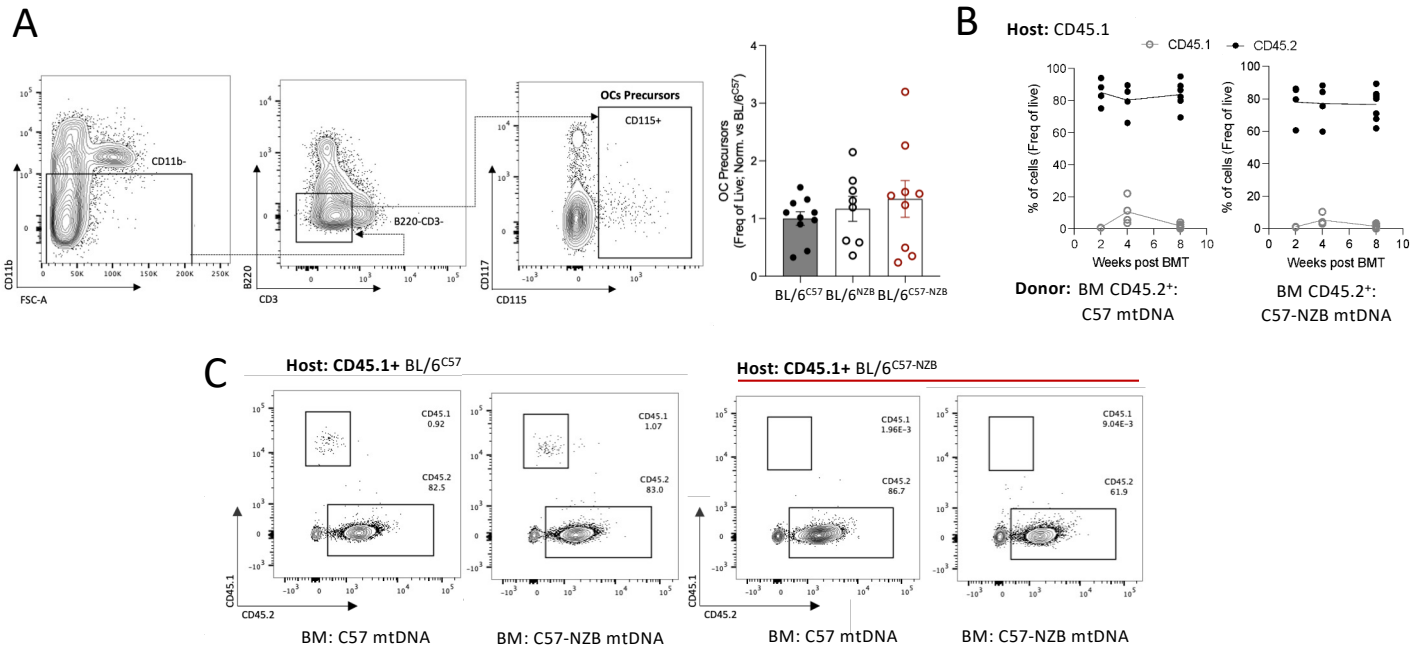

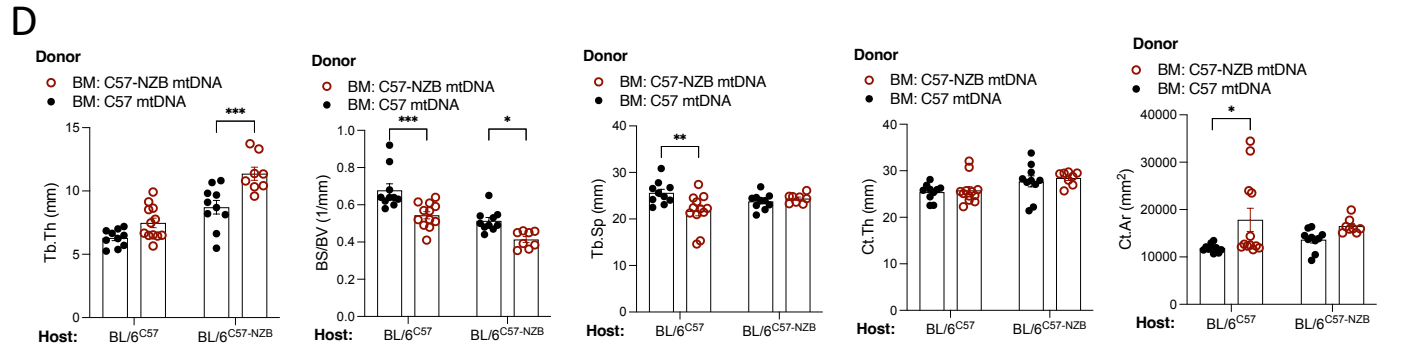

Supplementary Figure 1

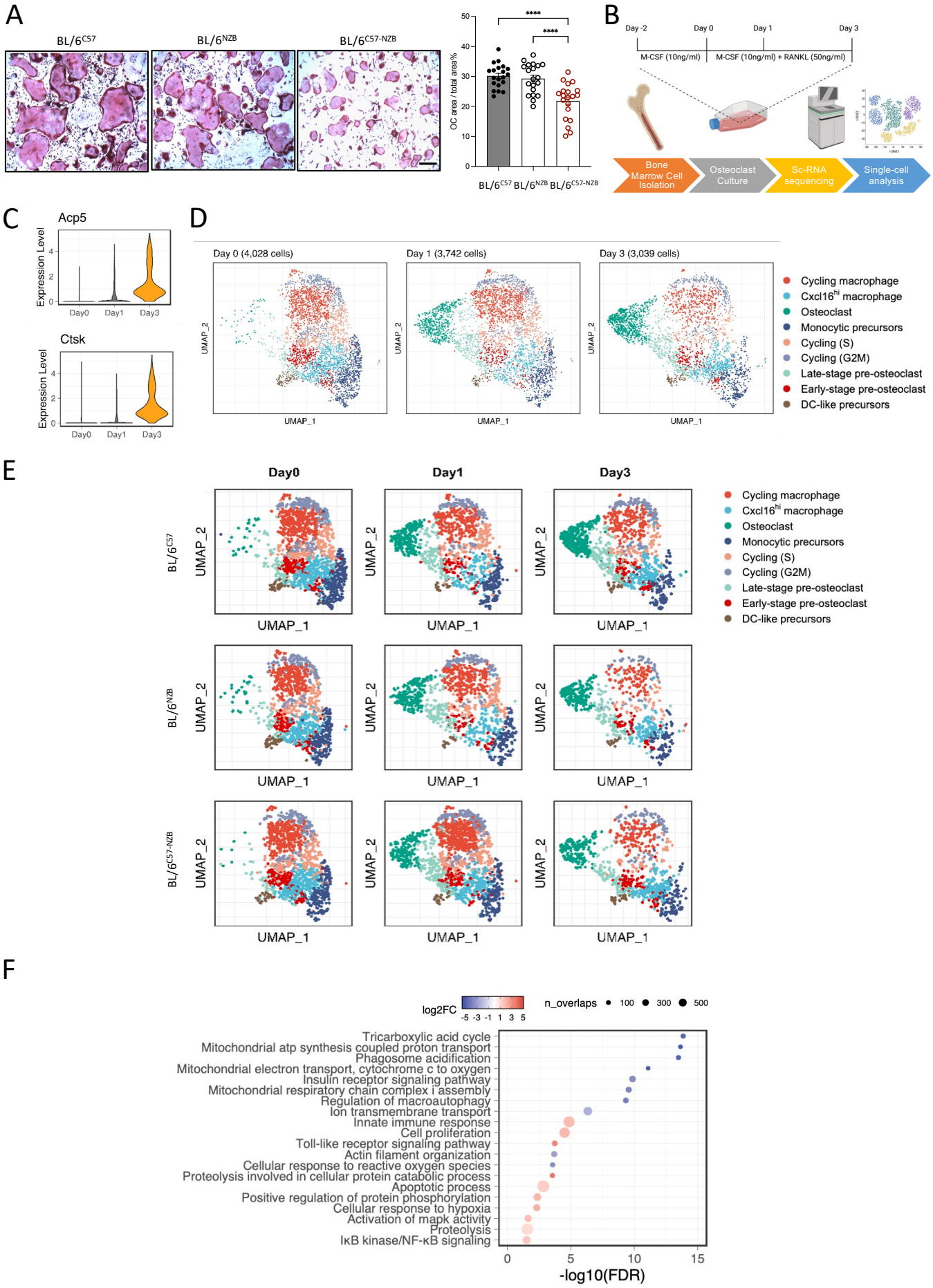
A
BL/6C57
BL/6NZB
BL/6C57-NZB
OC area / total area%
****
****
BL/6C57 BL/6NZB BL/6C57-NZB
B
Day -2
Day 0
Day 1
Day 3
M-CSF (10ng/ml)
M-CSF (10ng/ml) + RANKL (50ng/ml)
Bone Marrow Cell Isolation
Osteoclast Culture
Sc-RNA sequencing
Single-cell analysis
C
Acp5
Ctsk
Expression Level
Day0
Day1
Day3
D
Day 0 (4,028 cells)
Day 1 (3,742 cells)
Day 3 (3,039 cells)
UMAP_1
UMAP_2
Cycling macrophage
Cxcl16hi macrophage
Osteoclast
Monocytic precursors
Cycling (S)
Cycling (G2M)
Late-stage pre-osteoclast
Early-stage pre-osteoclast
DC-like precursors
E
Day0
Day1
Day3
BL/6C57
BL/6NZB
BL/6C57-NZB
F
log2FC
n_overlaps
Tricarboxylic acid cycle
Mitochondrial atp synthesis coupled proton transport
Phagosome acidification
Mitochondrial electron transport, cytochrome c to oxygen
Insulin receptor signaling pathway
Mitochondrial respiratory chain complex i assembly
Regulation of macroautophagy
Ion transmembrane transport
Innate immune response
Cell proliferation
Toll-like receptor signaling pathway
Actin filament organization
Cellular response to reactive oxygen species
Proteolysis involved in cellular protein catabolic process
Apoptotic process
Positive regulation of protein phosphorylation
Cellular response to hypoxia
Activation of mapk activity
Proteolysis
IκB kinase/NF-κB signaling
-log10(FDR)

Figure 2

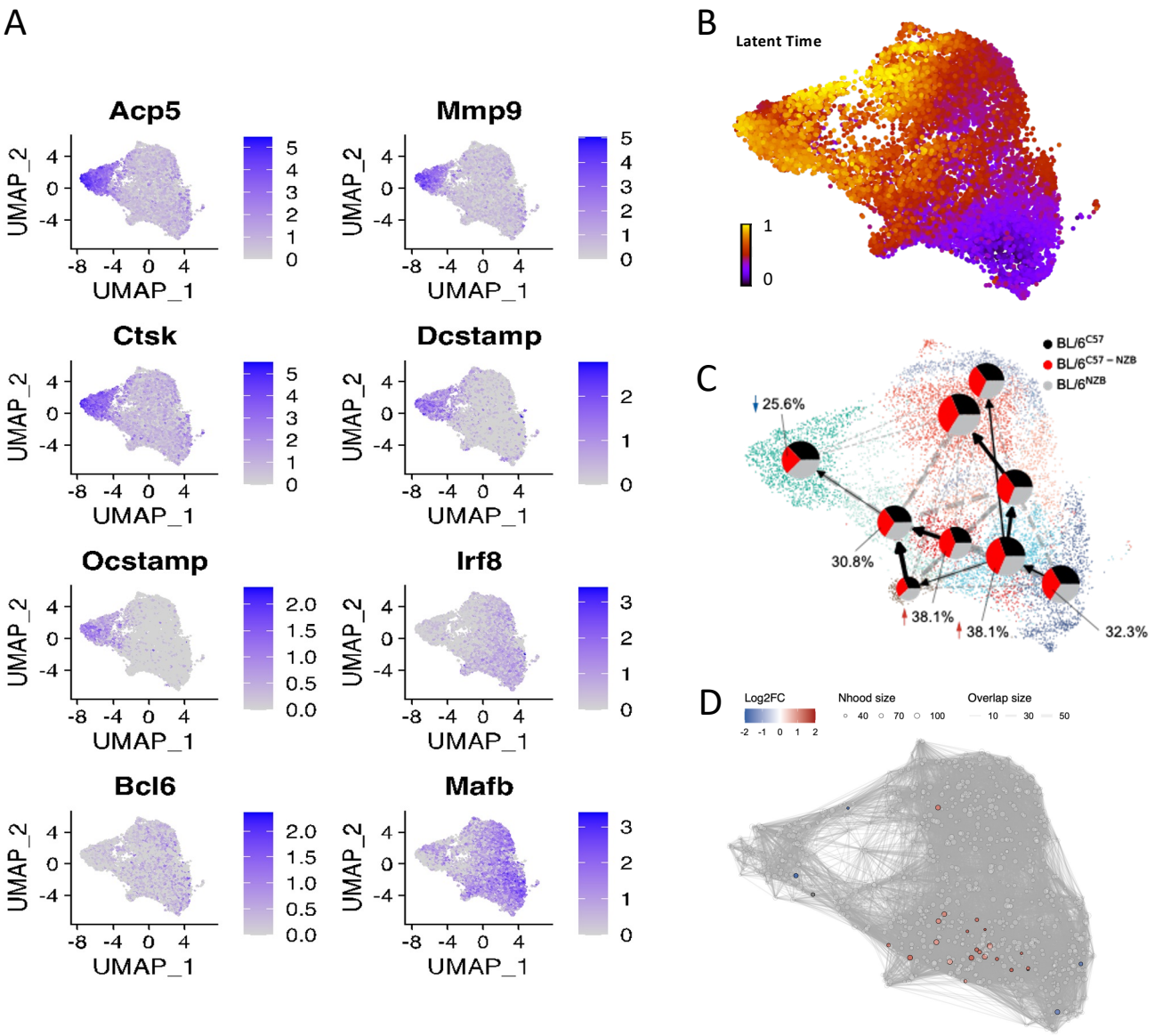

Supplementary Fig. 2

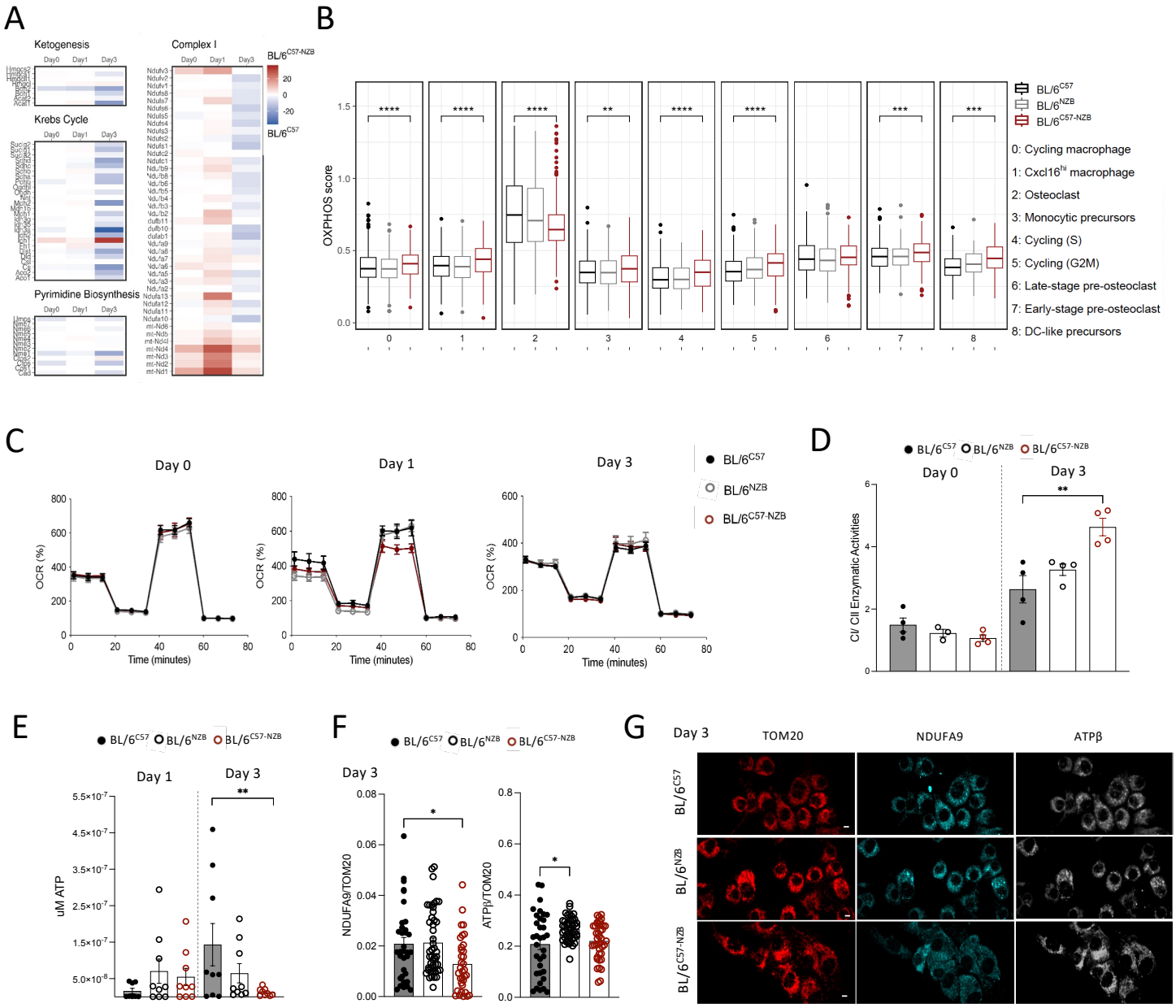
A
Ketogenesis
Krebs Cycle
Pyrimidine Biosynthesis
Complex I
Day0
Day1
Day3
BL/6C57-NZB
BL/6C57
B
OXPHOS score
BL/6C57
BL/6NZB
BL/6C57-NZB
0: Cycling macrophage
1: Cxcl16hi macrophage
2: Osteoclast
3: Monocytic precursors
4: Cycling (S)
5: Cycling (G2M)
6: Late-stage pre-osteoclast
7: Early-stage pre-osteoclast
8: DC-like precursors
C
Day 0
Day 1
Day 3
OCR (%)
Time (minutes)
D
Day 0
Day 3
CI/ CII Enzymatic Activities
E
Day 1
Day 3
uM ATP
F
Day 3
NDUFA9/TOM20
ATPβ/TOM20
G
Day 3
TOM20
NDUFA9
ATPβ

Figure 3

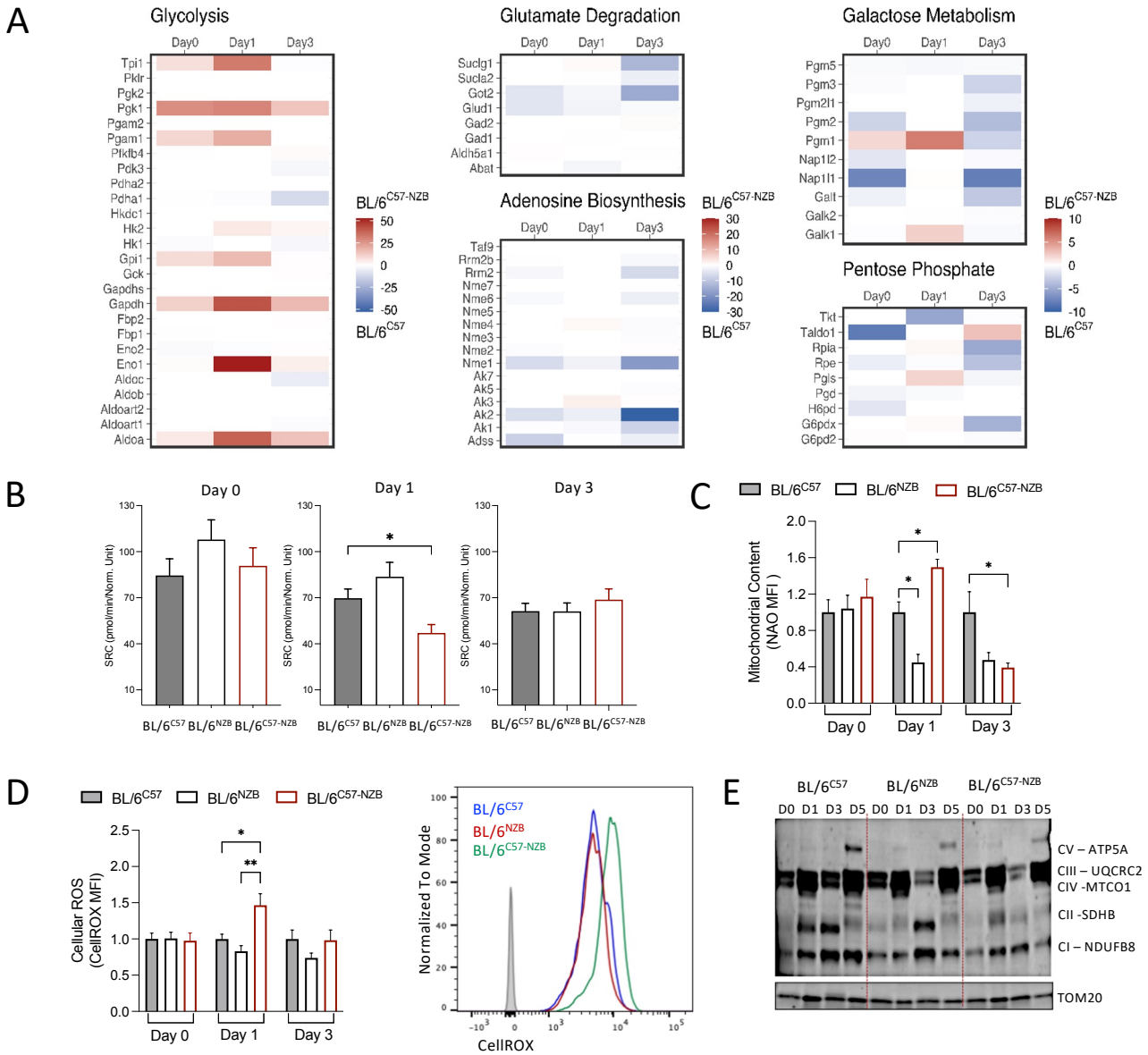

Supplementary Fig. 3

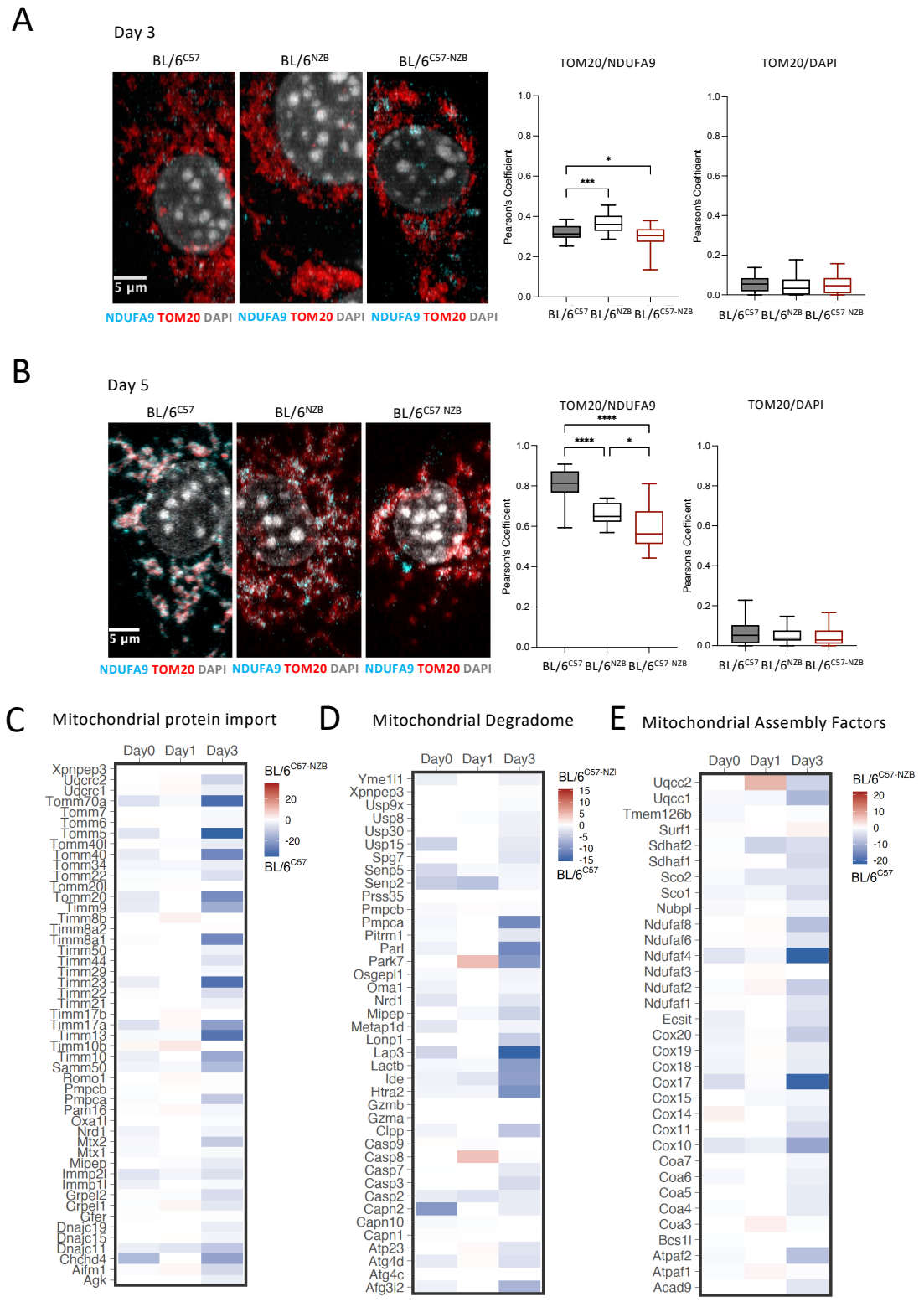
A
Day 3
BL/6C57
BL/6NZB
BL/6C57-NZB
5 µm
NDUFA9 TOM20 DAPI
TOM20/NDUFA9
TOM20/DAPI
Pearson's Coefficient
B
Day 5
C
Mitochondrial protein import
D
Mitochondrial Degradome
E
Mitochondrial Assembly Factors
Day0 Day1 Day3

Figure 4

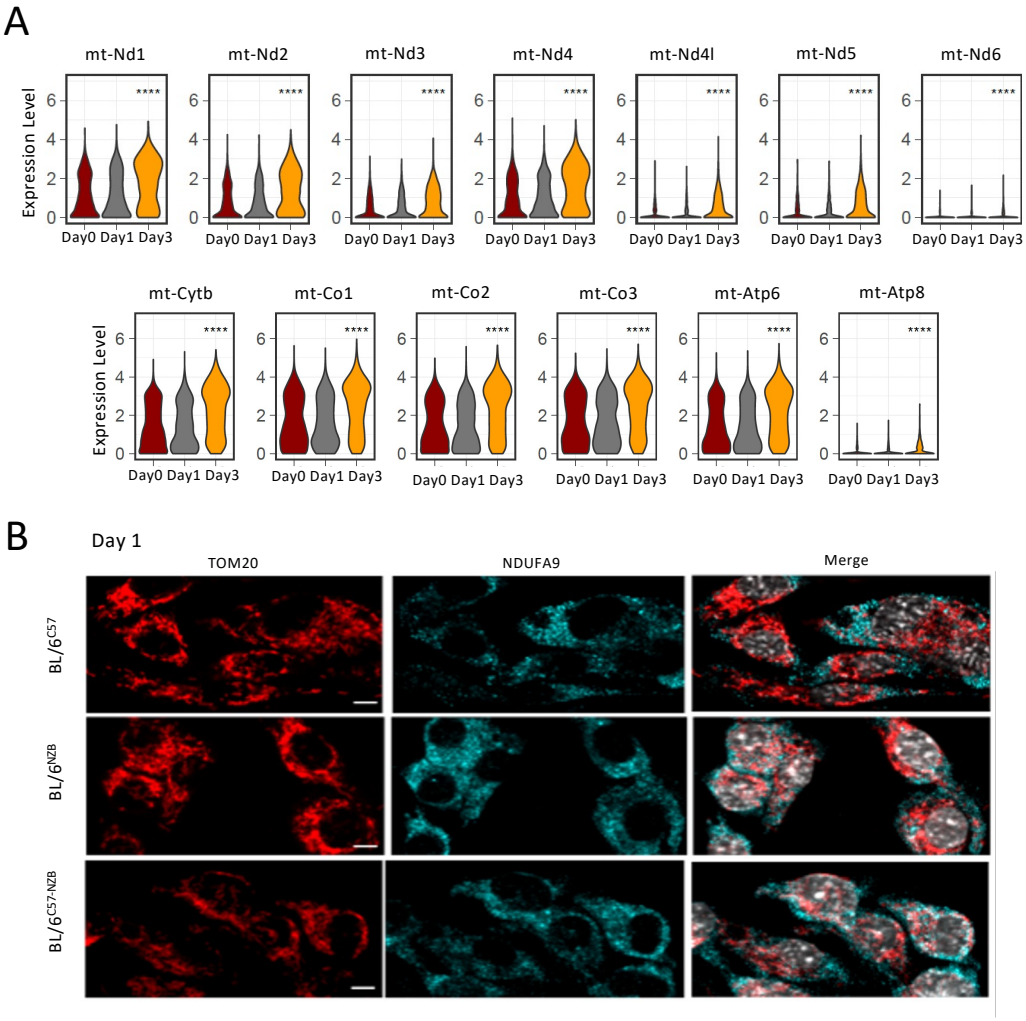

Supplementary Fig. 4

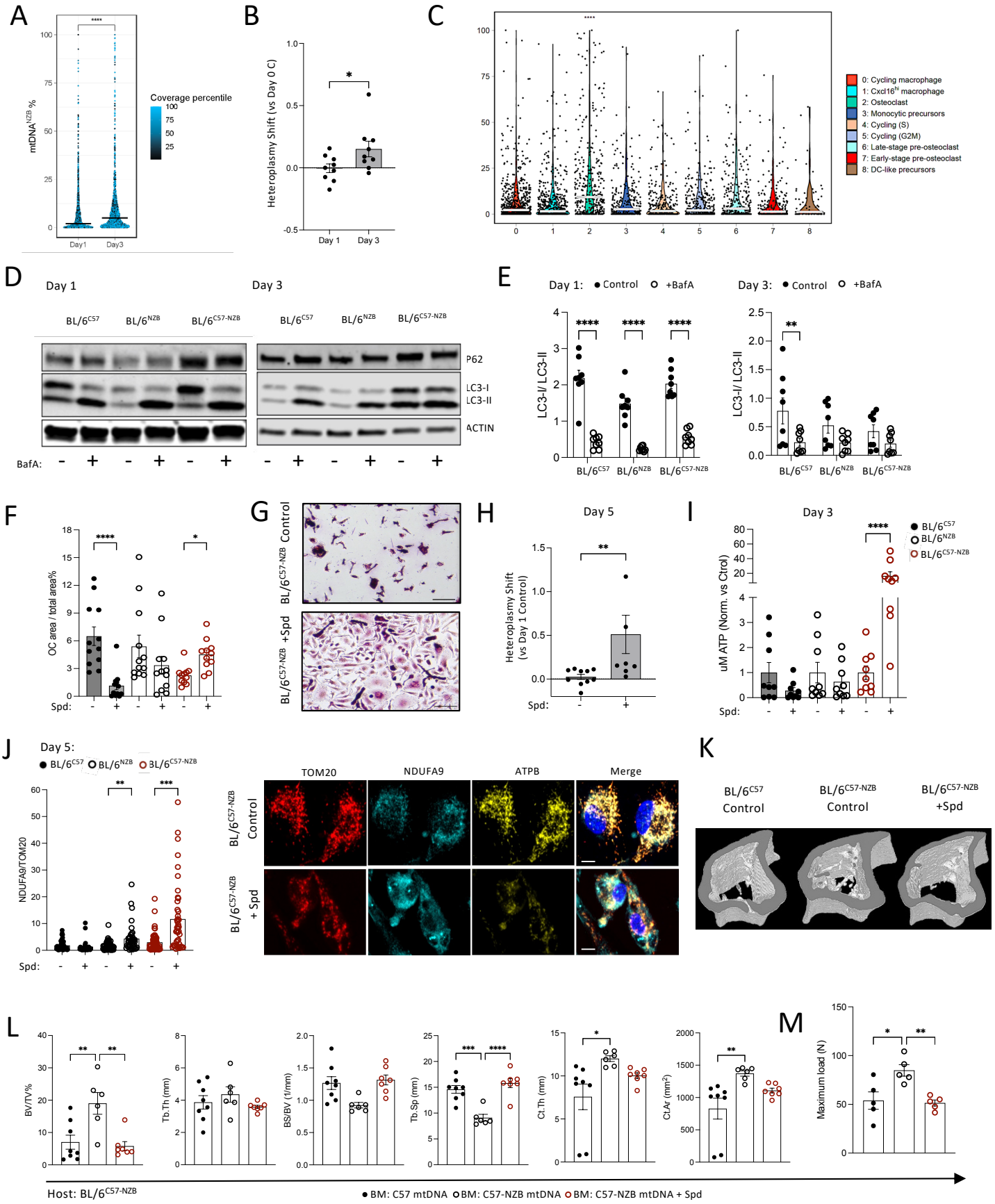
A
mtDNA^NZB %
Coverage percentile
Day1
Day3
B
Heteroplasmy Shift (vs Day 0 C)
Day 1
Day 3
C
0: Cycling macrophage
1: Cxcl16^hi macrophage
2: Osteoclast
3: Monocytic precursors
4: Cycling (S)
5: Cycling (G2M)
6: Late-stage pre-osteoclast
7: Early-stage pre-osteoclast
8: DC-like precursors
D
Day 1
Day 3
BL/6^C57
BL/6^NZB
BL/6^C57-NZB
P62
LC3-I
LC3-II
ACTIN
BafA:
E
Day 1: Control +BafA
Day 3: Control +BafA
LC3-I/ LC3-II
F
OC area / total area%
Spd:
G
Control
+Spd
H
Day 5
Heteroplasmy Shift (vs Day 1 Control)
I
Day 3
uM ATP (Norm. vs Ctrl)
J
Day 5:
NDUFA9/TOM20
TOM20
NDUFA9
ATPB
Merge
K
BL/6^C57 Control
BL/6^C57-NZB Control
BL/6^C57-NZB +Spd
L
BV/TV%
Tb.Th (mm)
BS/BV (1/mm)
Tb.Sp (mm)
Ct.Th (mm)
Ct.Ar (mm²)
M
Maximum load (N)
Host: BL/6^C57-NZB
BM: C57 mtDNA
BM: C57-NZB mtDNA
BM: C57-NZB mtDNA + Spd

Figure 5

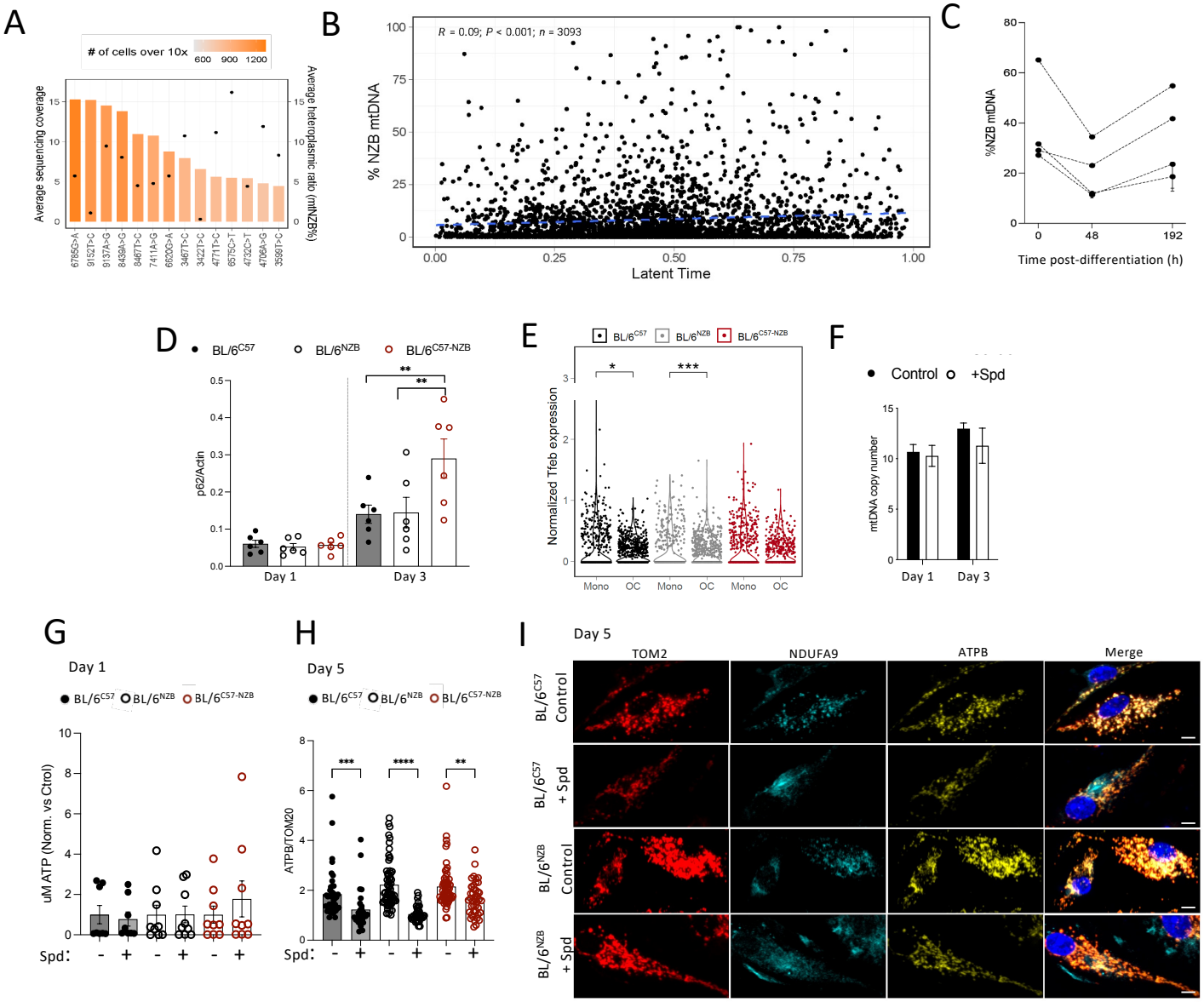

Supplementary Fig. 5

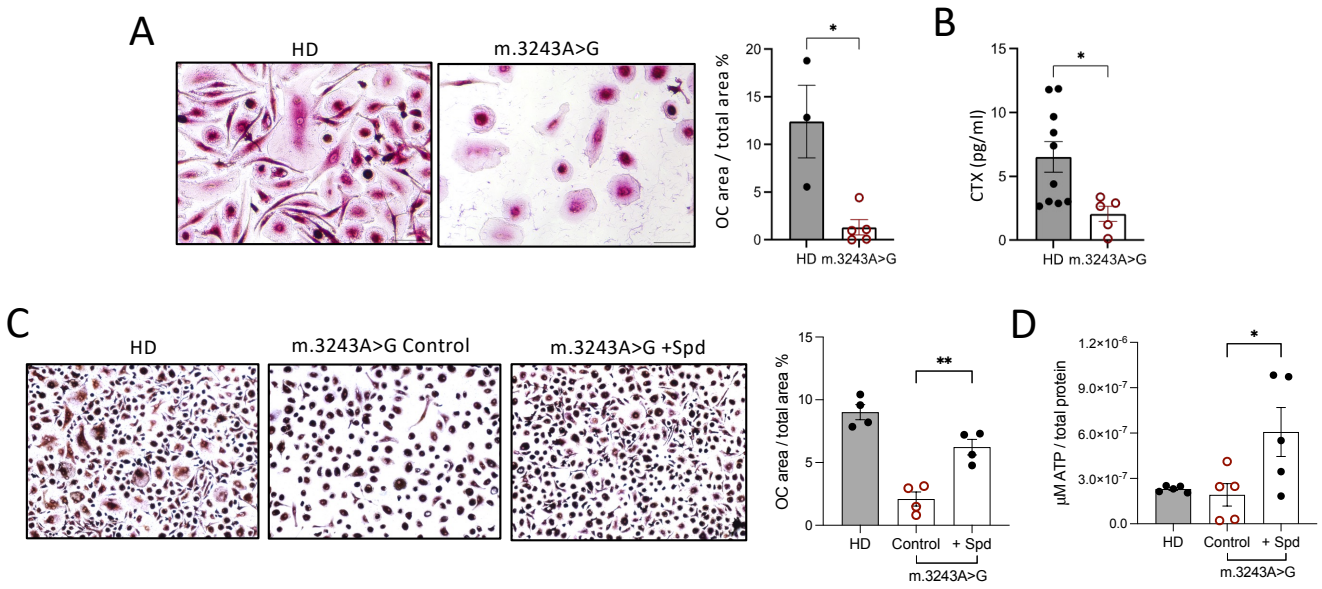
A
HD
m.3243A>G
OC area / total area %
20
15
10
5
0
*
HD m.3243A>G
B
CTX (pg/ml)
15
10
5
0
*
HD m.3243A>G
C
HD
m.3243A>G Control
m.3243A>G +Spd
OC area / total area %
15
10
5
0
**
HD
Control
+ Spd
m.3243A>G
D
µM ATP / total protein
1.2×10-6
9.0×10-7
6.0×10-7
3.0×10-7
0.0
*
HD
Control
+ Spd
m.3243A>G

Figure 6

Supplementary Table 1:

Algorithm 1: Bone Reconstruction

Input: $X \in R^{d \times h \times w}$, $x_{bone}, x_{cortical}, n_{frag} \in R$

Output: $V \in \{0,1\}^{d \times h \times w}$

1 Rotate and translate input volume to a standard position and orientation;

2 Extract the whole bone and cortical bones by thresholding: $V^0 \leftarrow nonzero(X - x_{bone})$, $V^1 \leftarrow nonzero(X - x_{cortical})$; /* 'nonzero' is a MATLAB function */

3 Remove the small fragments from the cortical bones' volume: $V^1 \leftarrow bwareaopen(V^1, n_{frag})$;

4 Remove the fibular bone (the second largest volume): $V^0 \leftarrow KeepRankedVol(V^0, -2), V^1 \leftarrow KeepRankedVolume(V^1, 1)$;

5 Dilate and erode the cortical bone to fill the hole inside: $V^1 \leftarrow SerialDilateErode(V^1, [12, -12])$;

6 Intersect the two volumes: $V \leftarrow V^0 \cap V^1$;

7 Return V.

Algorithm 2: Keep Ranked Volume

Input: $V^i \in \{0,1\}^{d \times h \times w}$, $k \in Z$

Output: $V^o \in \{0,1\}^{d \times h \times w}$

1 Find and count the connected components: $V^{cc} \leftarrow bwconncomp(V^i, 26)$; /* 'bwconncomp' is a MATLAB function */

2 Creates a label matrix corresponding to each connected component: $L^{cc} \leftarrow labelmatrix(V^{cc})$; /* 'labelmatrix' is a MATLAB function */

3 Calculate parameters of each component: $AreaProp \leftarrow regionprops(V^{cc}, 'Area')$; /* 'regionprops' is a MATLAB function */

Sort the areas: $(\cdot, index_{sort}) \leftarrow sort(AreaProp, 'descend')$;

4 Copy the volume: $V^o \leftarrow V^i$;

5 If $k > 0$ do:

6 Remove the components other than the kth largest volume: $V^o[L^{cc}! = k] \leftarrow 0$;

7 Else do:

8 Remove the components of the kth largest volume: $V^o[L^{cc} == k] \leftarrow 0$;

9 End

10 Return V^o.

11

Algorithm 3: Serial Dilate & Erode

Input: $V^i \in \{0,1\}^{d\times h\times w}$, $[t_1 \cdots t_k] \in Z^k$

Output: $V^o \in \{0,1\}^{d\times h\times w}$

Set the parameter size of structure element: $size$;

Initialize a structure element: $se \leftarrow strel('cube', size)$; /* 'strel' is a MATLAB */

Initialize the volume: $V^o \leftarrow V^i$;

Foreach $i \in [1, k] \cap Z$ do:

  Foreach $j \in [1, abs(t_i)] \cap Z$ do:

    If $t_i > 0$ do:

    Dilate the volume to fill the hole inside: $V^o \leftarrow imdilate(V^o, se)$;

      Elseif $t_i < 0$ do:

        Erode the volume to fit a specific size: $V^o \leftarrow imerode(V^o, se)$;

  End

End

Return V^o.

Algorithm 4: Count Area & Ratio

Input: $I^i \in R^{h\times w}$, $\tau \in R$, $n_{conn} \in Z$, $M^i \in \{0,1\}^{h\times w}$

Output: $M^r \in \{0,1\}^{h\times w}$, $a^r \in R^m$, $r^r \in R^m$

Normalize the input image: $I^o \leftarrow (I^i - I^i)/(I^i - I^i + 10^{-5})$;

Filter the image using a high passing filter: $I^o \leftarrow (1 - G) * I^i$; /* G is a gaussian filter kernel function */

Get the areas of the red channel: $M^r \leftarrow (I^o[\cdots,1] > \tau[1])\&(I^o[\cdots,2] < \tau[2])\&(I^o[\cdots,3] < \tau[3])$;

Find and count the connected components: $M^{cc} \leftarrow bwconncomp(M^i, 8)$; /* 'bwconncomp' is a MATLAB function */

Creates a label matrix corresponding to each connected component: $L^{cc} \leftarrow labelmatrix(M^{cc})$; /* 'labelmatrix' is a MATLAB function */

Calculate parameters of each component: $AreaProp \leftarrow regionprops(M^{cc}, 'Area')$; /* 'regionprops' is a MATLAB function */

Get the number of components: $m \leftarrow |AreaProp| - 1$;

Initialize the areas and ratios for each component: $a^r \leftarrow [0]_{m\times 1}$, $r^r \leftarrow [0]_{m\times 1}$

Foreach $i \in [1, m] \cap Z$ do:

$a^r[i] \leftarrow \sum(L^{cc} == i + 1) \cap M^r$;

$r^r[i] \leftarrow a^r[i]/\sum(L^{cc} == i + 1)$;

End

Return M^r, a^r, r^r.

Supplementary Table 2: Characteristics of individuals included in the study by m.3243A>G status.

Characteristics	m.3243A>G carriers N=76	Non-carriers, N=271,773
Age at recruitment, years	54 (13.3)	58 (13)
Female	30 (39)	147778 (54.4)
Individuals with heel BMD	76	271773
Individuals with DXA	15	46762
Blood heteroplasmy of m.3243A>G	0.088 (0.085)	-
Individuals with >5% heteroplasmy	76 (100)	-
Individuals 5-10% heteroplasmy	46 (60)	-
Individuals >10% heteroplasmy	30 (40)	-
Weight, kg	69.1 (21.6)	76.4 (21.0)

Median (IQR) for continuous data and n (%) for categorical data is displayed.

Supplementary Table 3: Association analysis (continuous phenotypes) of m.3243A>G with bone mineral density

Phenotype	Total n	n with >5% heteroplasmy	Effect size in g/cm² >5% heteroplasmy	p-value >5% heteroplasmy	n with >10% heteroplasmy	Effect size in g/cm² >10% heteroplasmy	p-value >10% heteroplasmy
Heel BMD	270568	76	-1.60×10^{-5}	0.99	30	-2.53×10^{-2}	0.29
Femur neck BMD	43129	13	-4.34×10^{-2}	0.19	6	-4.80×10^{-2}	0.29
L1-L4 BMD	42472	13	-4.56×10^{-2}	0.35	6	-5.08×10^{-2}	0.48
Total BMD	44494	14	-3.72×10^{-2}	0.20	7	-3.36×10^{-2}	0.41

Figure 2a: Results from linear regressions with BMD measures. Bonferroni corrected p-value < 0.0125.

Supplementary Table 4: Association analysis (binary phenotypes) of m.3243A>G with self-reported fracture and diabetes

Phenotype	n total	n >5% heteroplasmy	OR >5% heteroplasmy (95% CI)	p-value >5% heteroplasmy	n >10% heteroplasmy	OR >10% heteroplasmy(95% CI)	p-value >10% heteroplasmy
self-reported fracture	270247	76	0.528 (0.140, 1.41)	0.245	30	0.679 (0.0784, 2.69)	1.00
diabetes (Eur only)	253554	69	8.07 (4.86, 13.3)	8.22×10^{-15}	29	16.2 (7.24, 37.9)	2.74×10^{-12}

Figure 2b: Results from Fisher's exact test with self-reported fracture and diabetes.